Article

Neuron

Hallmarks of Alzheimer's Disease in Stem-Cell-Derived Human Neurons Transplanted into Mouse Brain

Highlights

- Human-mouse chimeric model of Alzheimer's disease
- PSC-derived human neurons grafted into an AD mouse
- Major degeneration and loss of human neurons in chimeric AD mice
- Absence of tangle pathology in degenerating human neurons in vivo

Authors

Ira Espuny-Camacho, Amaia M. Arranz, Mark Fiers, ..., Jean-Pierre Brion, Pierre Vanderhaeghen, Bart De Strooper

Correspondence

amaia.arranz@kuleuven.vib.be (A.M.A.), pvdhaegh@ulb.ac.be (P.V.), bart.destrooper@vib.be (B.D.S.)

In Brief

Espuny-Camacho, Arranz et al. show in this article a novel chimeric model of Alzheimer's disease generated using human neurons derived from pluripotent stem cells. This new chimeric model shows degeneration and major loss of human neurons without the presence of Tau tangles.

Espuny-Camacho et al., 2017, Neuron *93*, 1066–1081
March 8, 2017
http://dx.doi.org/10.1016/j.neuron.2017.02.001

CellPress

CellPress

Neuron
Article

Hallmarks of Alzheimer's Disease in Stem-Cell-Derived Human Neurons Transplanted into Mouse Brain

Ira Espuny-Camacho,[1,2,10] Amaia M. Arranz,[1,2,10,*] Mark Fiers,[1,2] An Snellinx,[1,2] Kunie Ando,[6] Sebastian Munck,[1,2,3] Jerome Bonnefont,[4] Laurie Lambot,[7] Nikky Corthout,[1,2,3] Lorna Omodho,[1,2] Elke Vanden Eynden,[1,2] Enrico Radaelli,[1,2] Ina Tesseur,[1,2] Selina Wray,[8] Andreas Ebneth,[9] John Hardy,[8] Karelle Leroy,[6] Jean-Pierre Brion,[6] Pierre Vanderhaeghen,[1,4,5,*] and Bart De Strooper[1,2,8,11,*]

[1]VIB Center for Brain and Disease Research, VIB-Leuven, 3000 Leuven, Belgium
[2]Center for Human Genetics, Universitaire ziekenhuizen and LIND, KU Leuven, 3000 Leuven, Belgium
[3]VIB Bio Imaging Core, KU Leuven, Herestraat 49, 3000 Leuven, Belgium
[4]Université Libre de Bruxelles (ULB), Institute for Interdisciplinary Research (IRIBHM), and ULB Institute of Neuroscience (UNI), 1070 Brussels, Belgium
[5]WELBIO, Université Libre de Bruxelles, 1070 Brussels, Belgium
[6]Laboratory of Histology, Neuroanatomy and Neuropathology and ULB Neuroscience Institute (UNI), Université Libre de Bruxelles, 1070, Brussels, Belgium
[7]Laboratory of Neurophysiology and ULB Neuroscience Institute (UNI), 808 Route de Lennik, 1070 Brussels, Belgium
[8]Institute of Neurology and Dementia Research Institute, University College London, Queen Square, WC1N 3BG London, UK
[9]Neuroscience Department, Johnson & Johnson Pharmaceutical Research and Development, Janssen Pharmaceutica, Turnhoutseweg 30, 2340 Beerse, Belgium
[10]Co-first author
[11]Lead Contact
*Correspondence: amaia.arranz@kuleuven.vib.be (A.M.A.), pvdhaegh@ulb.ac.be (P.V.), bart.destrooper@vib.be (B.D.S.)
http://dx.doi.org/10.1016/j.neuron.2017.02.001

SUMMARY

Human pluripotent stem cells (PSCs) provide a unique entry to study species-specific aspects of human disorders such as Alzheimer's disease (AD). However, in vitro culture of neurons deprives them of their natural environment. Here we transplanted human PSC-derived cortical neuronal precursors into the brain of a murine AD model. Human neurons differentiate and integrate into the brain, express 3R/4R Tau splice forms, show abnormal phosphorylation and conformational Tau changes, and undergo neurodegeneration. Remarkably, cell death was dissociated from tangle formation in this natural 3D model of AD. Using genome-wide expression analysis, we observed upregulation of genes involved in myelination and downregulation of genes related to memory and cognition, synaptic transmission, and neuron projection. This novel chimeric model for AD displays human-specific pathological features and allows the analysis of different genetic backgrounds and mutations during the course of the disease.

INTRODUCTION

Alois Alzheimer described in 1906 the main pathological hallmarks of Alzheimer's disease (AD): amyloid-β (Aβ) plaques, neurofibrillary pathology and tangles, astrogliosis, and neuronal loss (Alzheimer, 1906). Cerebrovascular amyloid angiopathy, microgliosis, inflammation, and major synaptic alteration are other pathological features of AD (Katzman, 1986; McGeer et al., 1988; Crews and Masliah, 2010; Spillantini and Goedert, 2013).

The amyloid hypothesis links abnormally folded Aβ peptides in a linear and causal cascade to the other disease hallmarks, including neuronal tangle formation and neuronal cell death (Hardy and Selkoe, 2002; critique in De Strooper and Karran, 2016). This hypothesis has provided the theoretical basis for the generation of numerous animal models, diagnostics, and therapeutics for AD. However, evolving insights have made increasingly clear that a more complex theory and more elaborate in vivo models are needed to understand the long prodromal phase of the disease (De Strooper and Karran, 2016). Rodent AD models (Ashe and Zahs, 2010; LaFerla and Green, 2012) usually overexpress mutated forms of the familial AD (FAD)-causing genes *APP* and/or *PSEN*, leading to extensive amyloid plaque deposition, Aβ-associated neuroinflammation, and some synaptic dysfunction. However, crucial aspects of the disease process, like neuronal tangle formation and severe neuronal loss, have never been convincingly demonstrated in rodents (Kokjohn and Roher, 2009; Morrissette et al., 2009; Crews and Masliah, 2010). The relevance of these genetic models to study sporadic AD, where patients do not carry mutations in *APP* or *PSEN*, is debated.

Human embryonic stem cells (ESCs) and patient-derived induced pluripotent stem cells (iPSCs) allow modeling of human neurological disease in a human genetic context (Brennand et al., 2015; Paşca et al., 2014; Vera and Studer, 2015; van den Ameele et al., 2014; Dolmetsch and Geschwind, 2011). Neurons derived from iPSCs of FAD patients showed altered $A\beta_{42}/A\beta_{40}$

ratio and abnormal Tau phosphorylation (Yagi et al., 2011; Israel et al., 2012; Shi et al., 2012; Kondo et al., 2013; Choi et al., 2014; Muratore et al., 2014; Hu et al., 2015). Recently, a three-dimensional, human neural stem-cell-derived culture (Choi et al., 2014) displayed Aβ plaque-like structures and Tau silver-positive aggregates (Choi et al., 2014). The cells overexpress exogenous *APP* and *PSEN* FAD genes. No cell loss was detected, and neuroinflammatory and vascular components of the disease are lacking in this in vitro model. It remains, indeed, crucial to complement in vitro approaches with in vivo experiments to study human neurons in the context of the diseased brain.

Neural precursors derived from pluripotent stem cells (PSCs) (reviewed in Suzuki and Vanderhaeghen, 2015) can be transplanted into the rodent brain, resulting in specific patterns of cortical neuronal maturation, connectivity, and synaptic activity, well beyond what can be achieved in a purely in vitro condition (Gaspard et al., 2008; Espuny-Camacho et al., 2013; Michelsen et al., 2015). We use here this approach to investigate whether Aβ species generated in an AD mouse model (Radde et al., 2006) are sufficient to induce full AD pathology in non-affected, genetically non-manipulated human neurons. This chimeric model presents numerous Aβ plaques and Aβ-associated neuroinflammation in the human transplant and, importantly, the transplanted neurons show remarkable signs of neurodegeneration that are not detected in the mouse host brain or in transplanted PSC-derived mouse neurons. Thus, human neurons respond to Aβ pathology differently than their murine counterparts in vivo.

RESULTS

Human-Grafted Neurons Integrate into the Mouse Brain and Are Exposed to Amyloid-β

We differentiated GFP-expressing human PSCs into cortical precursor cells in vitro to implant them as xenografts into the brains of newborn mice (Figure 1A; Figures S1E and S1F) (Espuny-Camacho et al., 2013). We used transgenic Tg (Thy1-APPSw,Thy1-PSEN1*L166P) 21Jckr, further called APP/PS1-21, mice (Radde et al., 2006) and crossed them with immunodeficient NOD.CB17-Prkdc^{scid}/J, further called NOD-SCID mice (Shultz et al., 1995), to generate AD mice or wild-type (WT) littermates suitable for grafting experiments (Espuny-Camacho et al., 2013). We additionally used GFP-expressing mouse neurons derived from murine PSCs as controls (Figures S2H and S2I) (Gaspard et al., 2008).

The cells present a normal karyotype (Figure S1D) or comparative genomic hybridization (CGH) array (data not shown) and undergo neuronal and telencephalic/cortical specification in vitro as attested by beta III tubulin, Tau, Tbr1, and Ctip2 staining (Figures S1A–S1C). The transplanted human neurons express GFP and human-specific markers, like HuNuclei (Figures S1G and S1H), and present cortical (Tbr1$^+$, CTIP2$^+$, Satb2$^+$, and Brn2$^+$), telencephalic (Foxg1$^+$), and mature neuronal (NeuN$^+$ and MAP2$^+$) identities (Figures 1B–1G; Figures S1I and S1J). Electron microscopy (EM), combined with GFP-immunogold labeling, shows numerous synapses between the human graft and the mouse host (Figures 1H and 1I). RNA sequencing (RNA-seq) analysis confirms broad expression of telencephalic, cortical, and glutamatergic, and some expression of GABAergic, astrocytic, and oligodendroglia genes (Figure S1K). Cholinergic, dopaminergic, or neural crest-derived cell identities are less abundant or absent (Figure S1K).

Aβ plaques are present in the AD mouse host brain (GFP negative), as assessed by Thioflavin, 6E10, and Congo red staining (arrows; Figures 1L–1N; Figures S2A–S2E). Congo red$^+$ plaques show birefringence when using plane-polarized light (Figure S2E). Importantly, Aβ plaques are detected within GFP$^+$ human neuronal clusters (arrowheads; Figures 1L–1M′; Figures S2A–S2B′, S2D, and S2E) and near single human neuronal cells integrated into the mouse host tissue (arrows; Figure 1N; Figure S2C). Aβ plaques within human clusters are more diffuse than mouse host dense-cored plaques and are significantly smaller (Figure 1O; 120 ± 6 μm^2 in mouse host; 88 ± 8 μm^2 in human grafts). No significant differences in number of Aβ plaques per unit surface are detected (Figure 1P; 40 ± 3 plaques/mm^2 in mouse host; 71 ± 16 plaques/mm^2 in human grafts). Aβ reactivity is, as expected, not observed in WT mice (Figures 1J and 1K).

Aβ plaque ultrastructure is very similar in the human transplants and in the mouse host: one or more cores of extracellular Aβ filaments (asterisks) surrounded by dystrophic neurites (DNs) (arrowheads) (Figures 1Q–1T). Immunogold labeling against human cell-specific markers, i.e., the GFP transgene or endogenous STEM121 marker, confirms that Aβ deposits (asterisk) and dystrophic neurites are within grafted human clusters (arrowheads point to immunogold particles; Figures S2F and S2G). PSC-derived mouse neurons transplanted under similar conditions also present Aβ plaques and DNs inside murine clusters (Figures S2H–S2K).

Thus, the transplanted neuronal clusters integrate into the mouse host tissue and are exposed to Aβ deposits produced by the AD mice.

Amyloid-β-Associated Neuroinflammation in the Human Neuronal Transplants

We detect GFAP$^+$ astrocytes (Figures 2A, 2B, 2E, and 2F) and Iba1$^+$ microglia cells (Figures 2C, 2D, 2G, and 2H) clustered around Thioflavin$^+$ Aβ deposits in mouse host tissue (GFP$^-$; arrows) and human grafts in AD mice (GFP$^+$; arrowheads). Significant increases in the number of GFAP$^+$ astrocytes and Iba1$^+$ microglial cells are seen in AD versus WT mice (Figures 2M and 2N), but neuroinflammation in mouse host and human transplants does not differ significantly. Microglia cells performing phagocytosis are detected (red arrowhead; Figure 2K). Astrocytes and microglial cells within human clusters are mostly of host origin as attested by the lack of GFP immunoreactivity (arrowheads; Figures 2I–2L). Ultrastructural analysis of astrocytes and microglia cells in human clusters in AD mice show an activated hypertrophic morphology with 76% and 74% of cells showing enlarged and/or phagocytic phenotypes, respectively (Figures 2P and 2R–2V). These phenotypes are rarely found in human grafts in WT mice (Figures 2O, 2Q, 2T, and 2V), indicating that the elicited immune response is induced by the Aβ-associated pathology and not a consequence of unexpected host-graft reactivity.

Thus, both grafted human neuronal clusters and mouse host tissue are similarly exposed to Aβ-associated neuroinflammatory responses characterized by astrocytic and microglial cell reactivity and recruitment to the Aβ plaque sites.

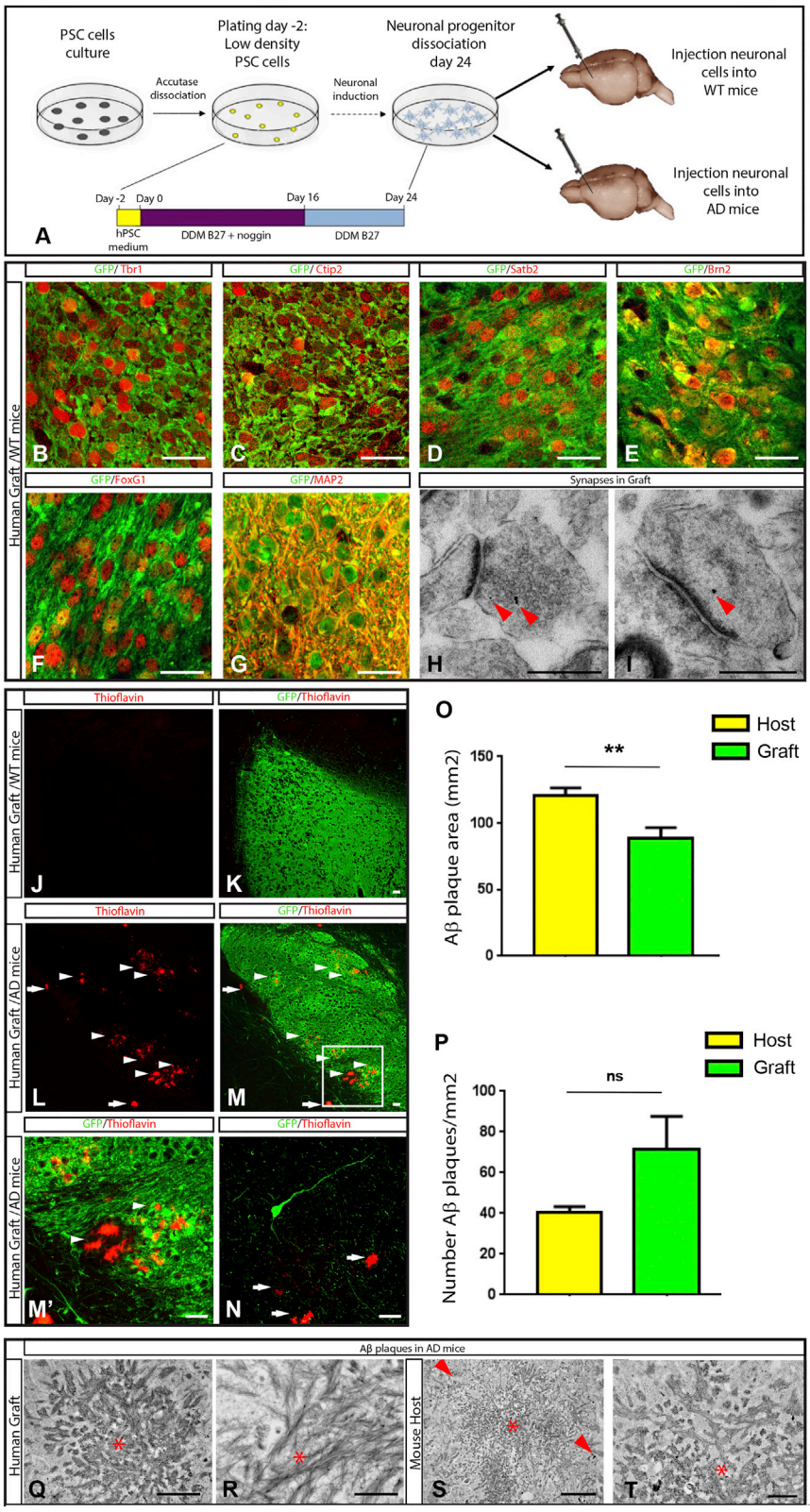

Figure 1. Human-Grafted Neurons Integrate into the Mouse Brain and Are Exposed to Aβ

(A) Schematic representation of the experimental outlay.

(B–G) GFP$^+$-grafted human neurons stained with the GFP antibody (green, B–G) and with the cortical deep layer markers Tbr1 (B) and CTIP2 (C), the upper layer markers Satb2 (D) and Brn2 (E), the telencephalic marker FoxG1 (F), or the mature neuronal marker MAP2 (G).

(H and I) Electron microscopy combined with GFP immunogold (arrowheads) shows synaptic contacts from the human transplant to the mouse host tissue (H) and reverse (I) 4 MPT.

(J–N) GFP (green) and Thioflavin-S (red) stainings show Aβ plaques within human transplants (arrowheads) and in mouse host tissue (arrows) in AD mice (L–N), but not in WT mice (J and K), 4 MPT. (M′) relates to (M). (N) shows an isolated GFP$^+$ neuron close to Aβ plaques (arrows).

(O and P) Quantification of Aβ plaque mean area (O) and of the number of Aβ plaques per area (P) in mouse host (n = 5) and human grafts (n = 5) in AD mice 4 MPT. Data are represented as mean ± SEM, Student's t test: **p < 0.01, n.s., non-significant.

(Q–T) EM images show Aβ deposits (asterisks) within human transplants or mouse host tissue in AD mice 4 MPT. Scale bars, 25 μm (B–G and J–N), 500 nm (H and I), 2 μm (Q), 1 μm (R), 10 μm (S), and 5 μm (T).

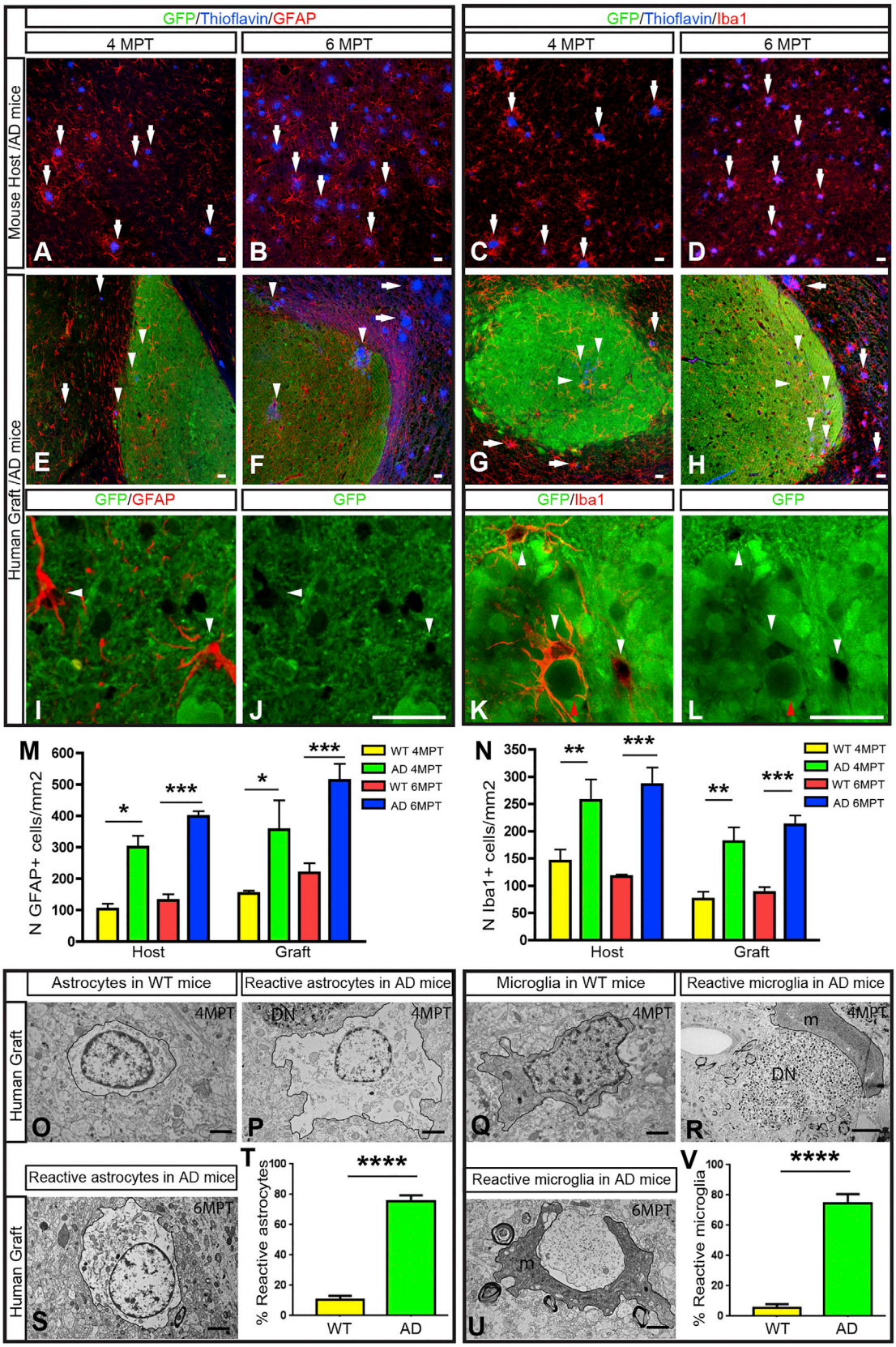

(legend on next page)

Extensive Neuritic Dystrophy and Alterations of Synaptic Markers Surrounding Aβ Plaques in Human Neuronal Transplants

We examined the grafted human neuronal clusters exposed to Aβ for signs of cellular or neuritic abnormalities. DN structures are found associated with Aβ plaques in both mouse host and human grafts in AD mice 4 months post-transplantation (MPT) (Figures 3A, 3B, 3D, and 3E), but not in WT mice (Figures 3C and 3F). DNs present a globular structure (Figures 3B and 3E) and a heterogeneous content of vesicles (red boxes), dense bodies (red arrowheads), mitochondria (blue boxes), and neurofilaments (green boxes) (Figures 3G–3N). Myelin alterations are also detected (arrowheads; Figures S4K and S4L).

Ubiquitin staining confirms the presence of DNs around Thioflavin+ Aβ plaques in mouse host tissue and human clusters 4 MPT (Figures 3O–3R) with 85% of Aβ plaques surrounded by DNs in human grafts versus 58% in mouse host (Figure 3S). DNs are also detected in human clusters in AD mice by GFP or human-specific STEM121 staining (arrowheads; Figures 3O, 4C, and 4J; Figures S2L and S2M) but are absent in human grafts in WT mice (Figures 4A and 4H). We observe abnormal accumulations of the presynaptic markers synaptophysin (SYP) and vesicular glutamate transporter 1 (VGlut1) around Aβ plaques in human clusters in AD mice (Figures 4C, 4D, 4J, and 4K), similar to the accumulations found in human AD brains (Brion et al., 1991) (Figures S3A–S3D). These accumulations are absent in human clusters in WT mice (Figures 4A, 4B, 4H, and 4I) and are less important in mouse host or in mouse neurons grafted in AD mice (Figures 4E, 4F, 4L, and 4M; Figures S3E–S3H), with 74% and 70% of Aβ plaques in human grafts surrounded by SYP and VGlut1+ structures, respectively, versus 23% and 39% in mouse host (Figures 4G and 4N). The dendritic marker MAP2 reveals an area devoid of staining around Aβ plaques in human clusters in AD mice (Figures 4O and 4P) that is minor in mouse host (Figures 4Q and 4R). The absence of MAP2 is mirrored by the accumulation of SYP^+ or Tau^+ structures around Aβ plaques (Figures S3I–S3P). The postsynaptic marker Homer1 confirms the reduction of dendritic staining around Aβ plaques in human neuronal clusters (Figures S3Q–S3T).

Thus, DNs surrounding Aβ plaques display abnormal accumulations of presynaptic and axonal proteins, while human dendritic and postsynaptic proteins become reduced. These neuritic changes are much more subtle in mouse host tissue or mouse neuronal clusters grafted in the AD mice.

Major Degeneration and Loss of Human Neurons In Vivo

Robust neuronal loss is a crucial AD hallmark lacking from existing animal models (Kokjohn and Roher, 2009; Morrissette et al., 2009; Crews and Masliah, 2010). Remarkably, the density of human neurons at 6 MPT, evaluated using GFP together with the pan nuclear marker TOPRO3 (Figures 5A–5F) or HuNuclei (Figures S4A–S4F), is much lower in transplants in AD mice (Figures 5D–5F) than in WT mice (Figures 5A–5C), although similar amounts of cells were injected. In contrast, nuclei density is similar in mouse host tissue in AD (Figures 5J–5L) versus WT mice (Figures 5G–5I).

Quantification shows that the density of mouse host tissue neurons is not significantly changed (98% in AD versus 100% in WT) while the density of human neurons in AD mice is reduced to 54% compared to WT animals (Figure 5M). The density of human neurons at 2 MPT—before Aβ plaques are detected—is not different between AD and WT animals (Figure 5M). Thus, the human cells integrate normally and similarly in WT and AD mouse brain following transplantation and cell loss occurs specifically in AD animals at later stages when Aβ pathology is present in vivo.

Semithin sections of human transplants stained with toluidine blue also show dense Aβ plaques, disorganized neuropil texture, and reduced neuronal density in AD mice (Figures 5N and 5O), while no such morphological alterations are seen in mouse host tissue and PSC-derived mouse grafts in AD mice. On the contrary, many healthy-appearing neurons are detected near Aβ plaques (Figures 5P and 5Q; Figures S4I and S4J). Ultrastructural analysis and quantification of neuron density confirm a significant decrease in the number of neurons in human grafts in AD at 6 MPT (Figure 5W; 1,463 ± 64 neurons/mm^2 in grafts in WT versus 344 ± 31 neurons/mm^2 in grafts in AD) and the absence of significant differences in mouse host tissue at this age (Figure 5W; 925 ± 47 neurons/mm^2 in host in WT versus 817 ± 37 neurons/mm^2 in host in AD).

Importantly, up to 33% of human neurons in AD mice show a necrotic phenotype (Figure 5X) characterized by electron lucent nuclei with highly dispersed chromatin, swelling of cytoplasm, and swelling and disintegration of cytoplasmic organelles (Figures 5S–5T′) (Nagańska and Matyja, 2001; Ueda et al., 2007; Burattini and Falcieri, 2013). Enlarged mitochondria with disrupted cristae (red arrowheads), large vacuoles (blue arrowheads), and even rupture of the nuclear membrane (green arrowheads)

Figure 2. Aβ-Associated Neuroinflammation in the Human Neuronal Grafts

(A–H) Representative micrographs of mouse host tissue (A–D) and GFP^+ human grafts (green, E–H) in AD mice. $GFAP^+$ astrocytes or $Iba1^+$ microglia cells (red) are associated with $Thioflavin^+$ Aβ plaques (blue) 4 MPT and 6 MPT. Arrows and arrowheads show Aβ plaques in mouse host tissue and within human grafts, respectively.

(I–L) GFP^- astrocytes and microglial cells (arrowheads; I–L) are present inside human grafts. Notice host, GFP^-, reactive microglia in phagocytic state (red arrowhead; K).

(M and N) Quantification of the number of $GFAP^+$ astrocytes (M) or $Iba1^+$ microglia cells (N) per area in mouse host (WT: n = 3 animals 4 MPT, n = 4 animals 6 MPT; AD: n = 3 animals 4 MPT, n = 4 animals 6 MPT) and human grafts (WT: n = 3 animals 4 MPT, n = 4 animals 6 MPT; AD: n = 3 animals 4 MPT, n = 4 animals 6 MPT). Data are represented as mean ± SEM, two-way ANOVA with Bonferroni post-tests: *$p < 0.05$; **$p < 0.01$; ***$p < 0.001$.

(O–V) Ultrastructure of hypertrophic reactive astrocytes (P and S) and reactive microglia (R and U) in human grafts 4 MPT and 6 MPT in AD mice. Notice non-reactive astrocytes and microglia in WT mice (O and Q) and phagocytosing microglia adjacent to dystrophic neurites (R) or degenerating material (U) in human grafts in AD mice. The cytoplasm of these cells has been outlined (O–U). DN, dystrophic neurite; m, microglia. Quantification of the percentage of glial cells showing hypertrophic and/or phagocytic morphology in human grafts in WT (n = 3) and AD (n = 3) mice 6 MPT (T and V). Data are represented as mean ± SEM, Student's t test: ****$p < 0.0001$. Scale bars, 25 μm (A–L), 2 μm (P–S), and 5 μm (O and U).

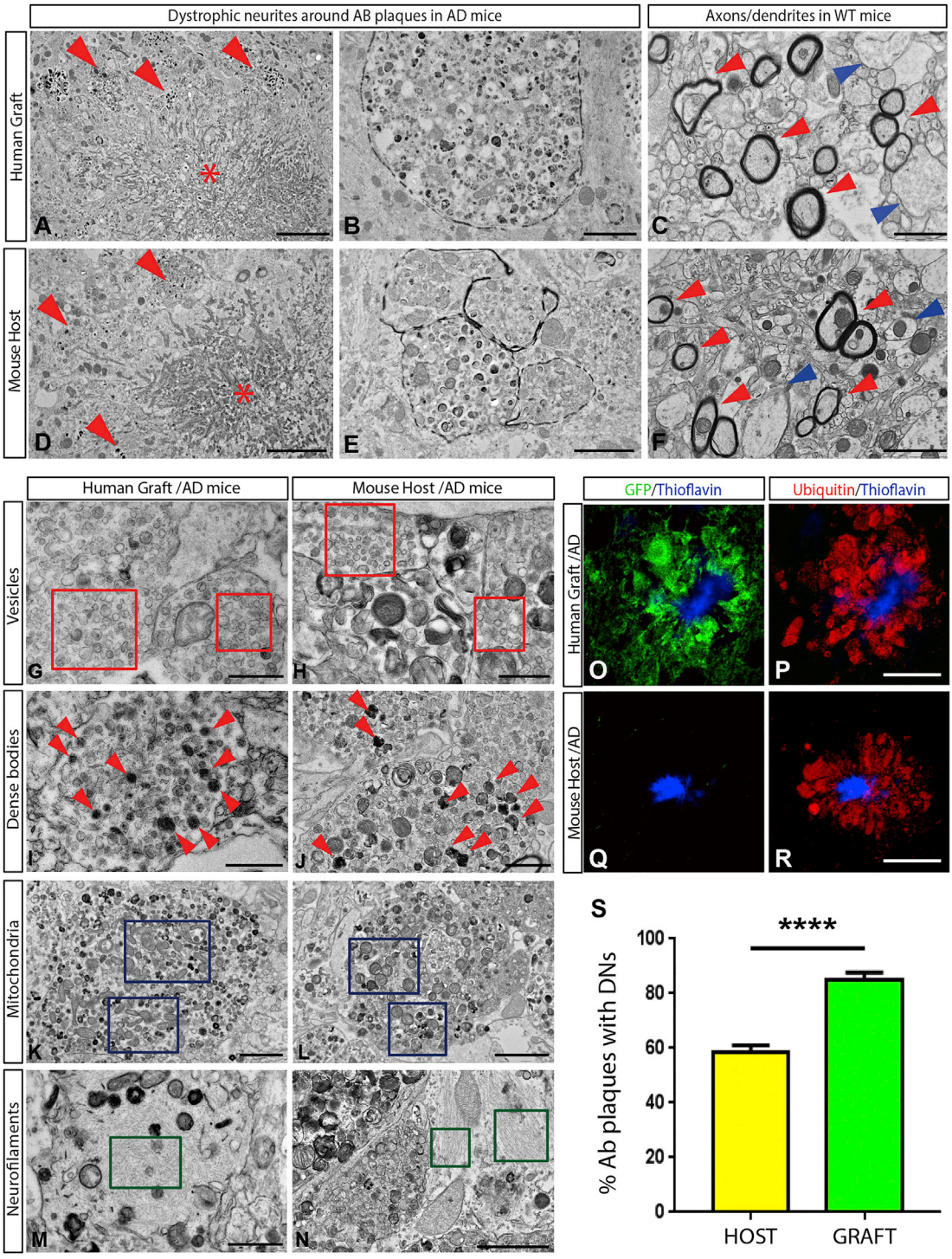

Figure 3. Neuritic Dystrophy Surrounding Aβ Plaques in Human Neuronal Transplants in AD Mice

(A–F) Ultrastructure of dystrophic neurites (DNs, arrowheads) around Aβ plaques (asterisks) in human grafts and mouse host tissue in AD mice (A, B, D, and E). Ultrastructure of axons (red arrowheads) and dendrites (blue arrowheads) in human grafts and mouse host tissue in WT mice (C and F).

(G–N) Heterogeneous content of DNs in human grafts and mouse host: accumulations of vesicles (red boxes; G and H), dense bodies (arrowheads; I and J), mitochondria (blue boxes; K and L), and neurofilaments (green boxes; M and N).

(O–R) Ubiquitin$^+$ DNs (red) around Thioflavin$^+$ Aβ plaques (blue) in GFP$^+$ human grafts (green in O and P) and mouse host tissue (Q and R) in AD mice 4 MPT.

(S) Quantification of the percentage of Aβ plaques surrounded by ubiquitin$^+$ DNs in mouse host (n = 5) and human grafts (n = 5) in AD animals 4 MPT. Data are represented as mean ± SEM, Student's t test: ****$p < 0.0001$. Scale bars, 25 μm (O–R), 5 μm (A), 2 μm (B, D–F, J–L, and N), 1 μm (C, G, I, and M), and 500 nm (H).

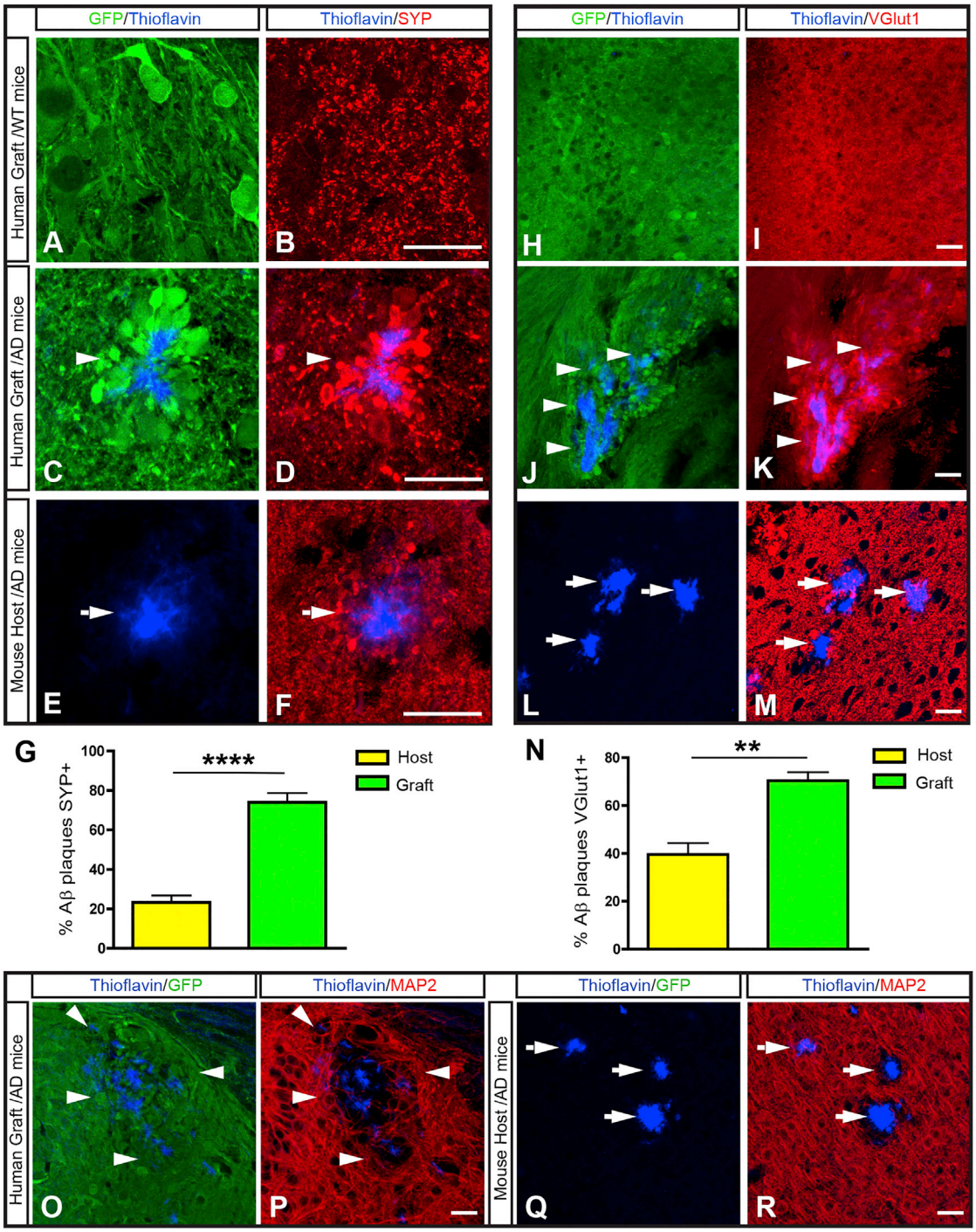

Figure 4. Specific Accumulation of Neuritic/Synaptic Markers around Aβ Plaques in Human Neuronal Grafts in AD Mice

(A–N) Representative images of human clusters in WT and AD mice and AD mouse host tissue stained with GFP (green; A, C, E, H, J, and L), Thioflavin (blue; A–F and H–M), and synaptophysin (SYP, red; B, D, and F) or VGlut1 (red; I, K, and M) 4 MPT. SYP^+ and $VGlut1^+$ accumulations around Aβ plaques in GFP^+ human clusters in AD mice (arrowhead; D and K). Minor accumulations in mouse host tissue in AD mice (arrow; F and M). Quantification of the percentage of Aβ plaques surrounded by SYP^+ or $VGlut^+$ accumulations in mouse host (n = 5) and human grafts (SYP: n = 5, VGlut1: n = 4) in AD mice (G and N). Data are represented as mean ± SEM, Student's t test: $^{**}p < 0.01$; $^{****}p < 0.0001$.

(O–R) Representative images of human clusters and mouse host tissue in AD mice stained with GFP (green; O and Q), Thioflavin (blue; O–R), and MAP2 (red; P and R) 4 MPT. GFP^+ human clusters show lack of MAP2 around Aβ plaques (arrowheads), while minor effects were detected in the mouse host tissue (arrows). Scale bars, 25 μm (A–R).

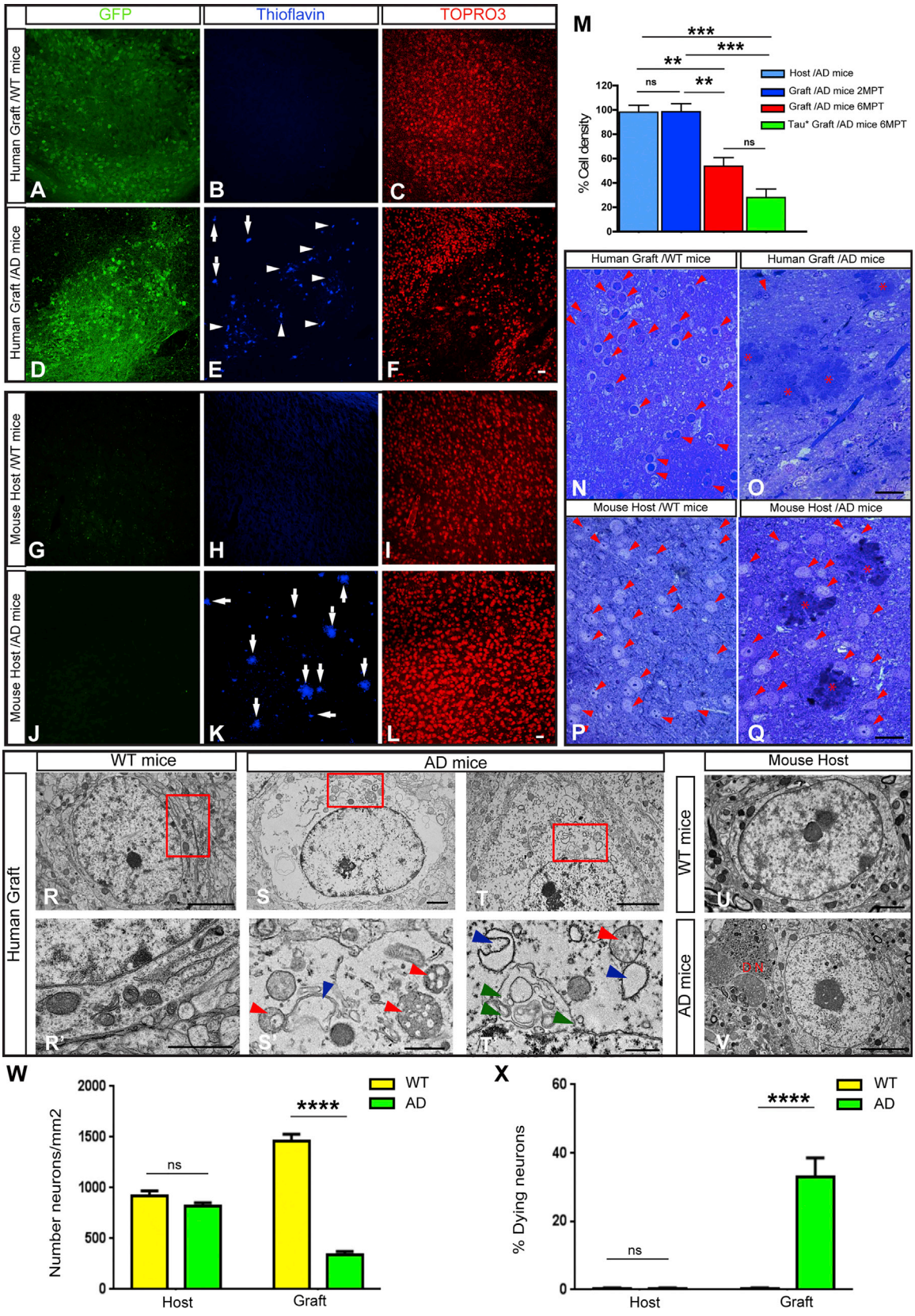

(legend on next page)

are also seen (Figures 5S′–5T′). However, such phenotypes are completely absent in human neurons in WT mice (Figures 5R, 5R′, and 5X). The effects appear human specific as no signs of degeneration are observed in mouse host tissue or in PSC-derived mouse neurons in AD mice (Figures 5V and 5X; Figure S4N). Apoptotic cell death does not contribute strongly to the cell loss at this stage as no increased caspase-3-activated staining (data not shown) or TUNEL labeling is observed (Figures S4O–S4Z).

Overall, the human grafts exposed to Aβ undergo major neuronal loss and neurodegeneration in vivo via a necrosis-mediated mechanism. Moreover, this effect is species specific as mouse host neurons or grafted mouse neurons exposed to the same Aβ load do not undergo degeneration.

Gradual Appearance of the 4R Tau Splicing Form in Human Neurons In Vivo

Adult murine brain mainly expresses the 4R Tau isoform containing four microtubule-binding repeats. During human brain embryonic development, only the 3R splice form of Tau is detected, while the adult human brain expresses 3R and 4R Tau splice forms in a 1:1 ratio (Goedert and Jakes, 1990). We thus studied the expression pattern of Tau using specific antibodies raised against 3R or 4R Tau splice forms (Figures S5M and S5N). After 2 and 4 MPT, 3R Tau is expressed, but 4R Tau is detected only in 0.7% of the human neurons (GFP^+ or $STEM121^+$), while 4R Tau is widely expressed in mouse host tissue (Figures 6A–6B′, 6E–6F′, and 6M; Figures S5A–S5C). However, at 6 MPT, 89% of the human neurons express high levels of 4R together with 3R Tau (arrows; Figures 6I–6J′ and 6M; Figures S5G–S5I). In addition, RNA-seq analysis of human grafts in old animals (8 MPT) shows a 3R/4R Tau expression close to 1, similar to the ratio in adult human brain (Figure 6N).

We wondered whether the appearance of 4R Tau could be accelerated in our model using two human iPSC lines derived from a patient carrying the pathogenic Tau mutation Ex10+16 (further indicated as Tau*) (Sposito et al., 2015). This mutation is considered to favor 4R Tau expression and causes Frontotemporal dementia (FTD) (Hutton et al., 1998). Following in vivo transplantation, human Tau* neurons ($HuNCAM^+$) showed no 4R Tau expression at 2 MPT (Figures 6C–6D′). However, at 4 MPT 37% of the human Tau* neurons expressed 4R together with 3R Tau isoforms (arrows; Figures 6G–6H′ and 6M; Figures S5D–S5F) in agreement with previous findings in vitro (Sposito et al., 2015). At 6 MPT, 84% of Tau* neurons highly expressed 4R together with 3R Tau (arrows; Figures 6K–6L′ and 6M; Figures S5J–S5L).

Human Tau* neurons transplanted into the AD mouse brain show similar phenotypes as described above. We detect numerous Aβ plaques within the grafts (Figures S6A–S6H) and DNs (Figures S6I and S6J). SYP^+ and $VGlut^+$ accumulations are surrounding Aβ plaques (Figures S6K–S6L′). Importantly, the density of grafted human Tau* neurons near Aβ plaques is reduced to 28% compared to WT animals (Figure 5M; Figures S6M–S6R). Toluidine blue-stained semithin sections (Figures S6S and S6T) and EM analysis (Figures S6U and S6V) confirm neuronal loss and necrosis that are not seen in human Tau* neurons in WT mice.

Thus, major AD human-specific pathological hallmarks are reproduced with iPSC-derived human neurons from a FTD patient transplanted into AD mice.

Presence of Pathological Tau Species in Human Neurons In Vivo

We analyzed Tau pathology in the grafted human neurons. $AT8^+$ hyperphosphorylated forms of Tau are found in the cell bodies of human neurons and human Tau* neurons (arrowheads; Figures 7B and 7E) and in DNs adjacent to Aβ plaques (arrowheads; Figures 7C and 7F) at 8 MPT in AD mice. Staining is similar to that found in AD human brain (arrows; Figures S7J–S7O) and in AD mouse tissue (arrowheads; Figures 7H and 7I). In fact, more than 95% of Aβ plaques show $AT8^+$ DNs in mouse host, human grafts, and human Tau* grafts (Figure 7S).

Figure 5. Neurodegeneration and Neuronal Loss in Human, but Not in Murine, Transplants in AD Mice

(A–L) Representative images of human grafts (A–F) and mouse host tissue (G–L) in WT and AD mice stained with GFP (green), Thioflavin (blue), and the nuclear marker TOPRO3 (red) 6 MPT. Areas devoid of $TOPRO3^+$ cells are evident within the human grafts in AD mice (F) together with abundant Aβ plaques within human clusters and in surrounding host tissue (arrowheads and arrows, E). In contrast, homogeneous staining of mouse nuclei is seen in AD mice (L), even in the presence of Aβ plaques (arrows, K). Human grafts and mouse host tissue in WT mice show homogeneous staining of nuclei (C and I) and no Aβ plaques (B and H).

(M) Percentage of relative cell density (number of nuclei per area) of mouse host tissue neurons (AD: n = 4 animals; WT: n = 4 animals), human neurons 2 MPT (AD: n = 4 animals; WT: n = 3 animals), human neurons 6 MPT (AD: n = 4 animals; WT: n = 4 animals), and human Tau* neurons 6 MPT (AD: n = 3 animals; WT: n = 3 animals) in AD animals compared to the density in WT animals expressed as 100%. Data are represented as mean ± SEM, one-way ANOVA with Bonferroni post-tests: $^{**}p < 0.01$, $^{***}p < 0.001$, n.s., non-significant.

(N–Q) Toluidine blue-stained semithin sections of human clusters and mouse host tissue in WT and AD mice 6 MPT. Human clusters in AD mice (O) show accumulation of dense Aβ plaques (asterisks), disorganized neuropil texture, and reduced neuronal density compared to human clusters in WT mice (N). AD mouse host tissue (Q) show accumulation of dense Aβ plaques (asterisks) but no gross changes in neuropil texture or reduced cell density compared to WT mouse host (P). Arrowheads point to neurons.

(R–V) Ultrastructure of grafted human and mouse host neurons in WT and AD mice 6 MPT. (R′), (S′), and (T′) relate to (R), (S), and (T). DN, dystrophic neurites. Signs of neurodegeneration consistent with necrosis are specifically observed in human neurons grafted in AD mice (S, S′, T, and T′) while no signs are observed in human neurons grafted in WT mice (R and R′) or in mouse host neurons (U and V). Red, blue, and green arrowheads point to degenerating mitochondria, vacuolar structures, and disrupted nuclear membranes, respectively.

(W) Quantification of neuronal density expressed as the number of neurons per area in mouse host (WT: n = 3, AD: n = 3) and human grafts (WT: n = 3, AD: n = 3) 6 MPT. Data are represented as mean ± SEM, two-way ANOVA with Bonferroni post-tests: $^{****}p < 0.0001$; n.s., non-significant.

(X) Quantification of the percentage of dying neurons in mouse host (WT: n = 3, AD: n = 3) and human grafts (WT: n = 3, AD: n = 3) 6 MPT. Data are shown as mean ± SEM, two-way ANOVA with Bonferroni post-tests: $^{****}p < 0.0001$; n.s., non-significant. Scale bars, 25 μm (A–L), 50 μm (N–Q), 5 μm (R, T, and V), 2 μm (S, U, and R′), and 1 μm (S′ and T′).

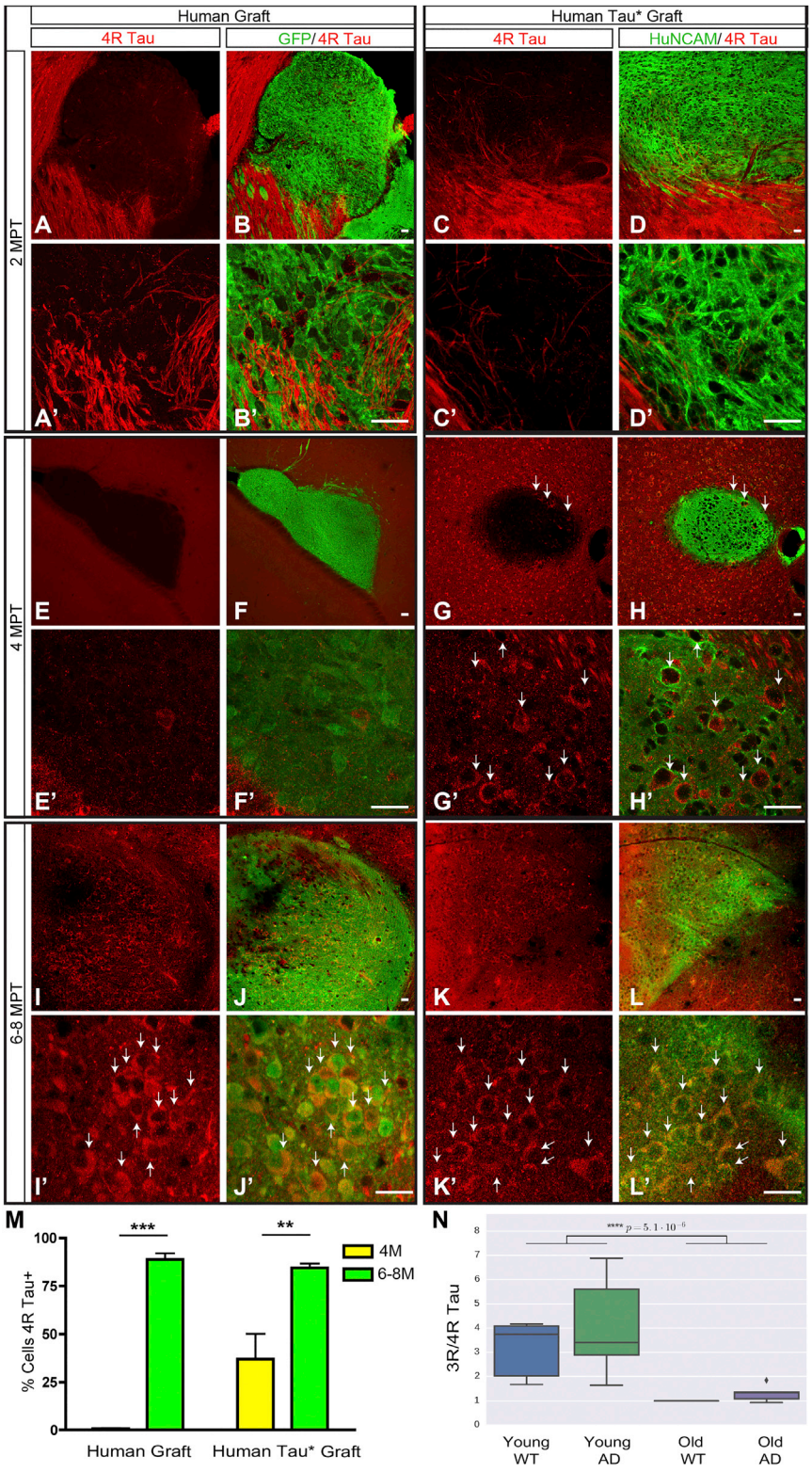

Figure 6. Temporal Pattern of 3R and 4R Tau Expression in Human Neurons Grafted In Vivo

(A–L′) Grafted human neurons (A, B, E, F, I, and J) detected with GFP (green) or grafted human Tau* neurons (C, D, G, H, K, and L) detected with HuNCAM (green) and stained for 4R Tau (red) after 2, 4, and 6 MPT. Higher-magnification images are shown in A′–L′. Arrows show 4R Tau$^+$ human neurons.

(M) Quantification of the percentage of 4R Tau$^+$ cells in human grafts (n = 3 animals 4 MPT; n = 6 animals 6–8 MPT) and human Tau* grafts (n = 4 animals 4 MPT; n = 2 animals 6–8 MPT). Data are represented as mean ± SEM, two-way ANOVA with Bonferroni post-tests: $^{**}p < 0.01$, $^{***}p < 0.001$.

(N) Quantification of the RNA-seq data for 3R/4R Tau ratio in human grafts in young (4–5 MPT) (n = 5 WT, 7 AD) and old (8 MPT) (n = 2 WT, 5 AD) animals. Results are shown as mean ± SEM, Student's t test: $^{***}p < 0.0001$. Scale bars, 25 μm (A–L′).

Importantly, MC1$^+$, which reveals a pathological Tau conformation, is also detected in few cell bodies of human neurons and human Tau* neurons (arrowheads; Figures 7K and 7N; Figures S7A–S7C′), and more than 96% of Aβ deposits show MC1$^+$ DNs at 8 MPT in human clusters in AD mice (arrowheads; Figures 7L, 7O, and 7T; Figures S7D–S7F′), similarly to human AD brain (arrows; Figures S7P–S7U) (Weaver et al., 2000). However, no MC1 staining is found in mouse host tissue in AD mice (Figures 7Q, 7R, and 7T; Figures S7G–S7I′), as previously described (Kokjohn and Roher, 2009; Morrissette et al., 2009). The lack of MC1 reactivity in AD mouse host is probably not explained by human specificity of the antibody as it also labels mouse Tau in a pericyte-deficient *APP* transgenic mouse model (Sagare et al., 2013). No AT8 or MC1$^+$ staining is detected in WT mice (Figures 7A, 7D, 7G, 7J, 7M, and 7P).

Cytoskeletal alterations with abnormal accumulation of straight 10-nm-wide neurofilaments are detected in DN of human neurons in AD mice 6–8 MPT (Figures S7V and S7V′). In addition, Hirano bodies, paracrystalline inclusions with an array of symmetrically organized 8–10 nm filaments, are also present (Figures S7W and S7W′). However, abnormal filaments in the form of paired helical filaments or twisted ribbons have not been detected.

These results show that even after 6–8 MPT the human neurons do not present definite tangle pathology although clear hyperphosphorylation and pathological conformational alterations of Tau are observed. Thus, there is major neurodegeneration even in the absence of full-spread tangle pathology in the human neurons.

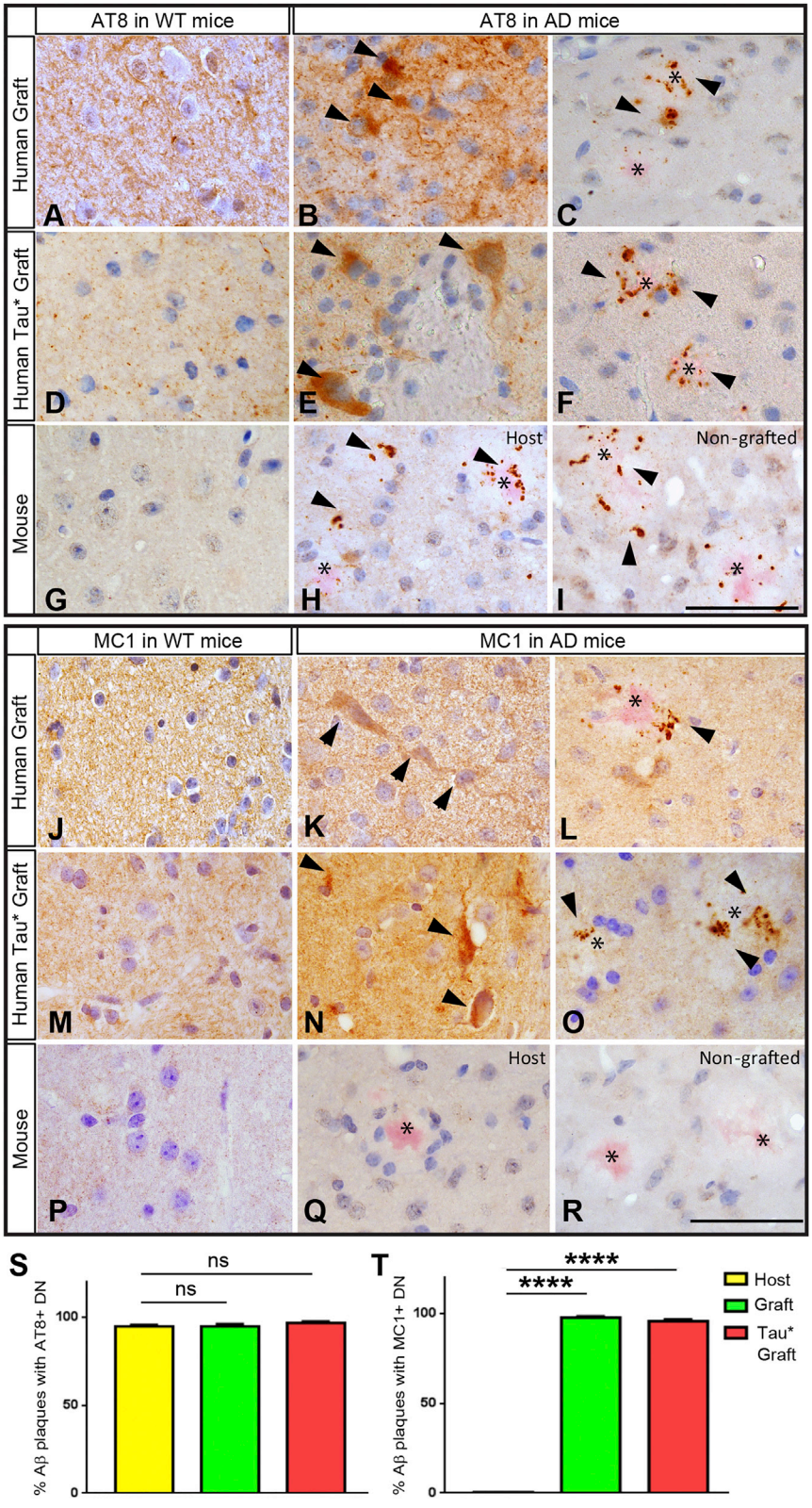

Figure 7. Tau Hyperphosphorylation and Abnormal Tau Conformational Changes in Grafted Human Neurons

(A–R) Immunohistochemistry with AT8 (brown; A–I) or MC1 (brown; J–R) of human grafts, human Tau* grafts, mouse host tissue, and non-grafted mouse brain tissue in WT and AD mice. AT8$^+$ neuronal cell bodies (arrowheads; B and E) and DNs around Congo red$^+$ Aβ deposits (pink, asterisks) (arrowheads; C, F, H, and I) in human grafts (B and C), human Tau* grafts (E and F), and mouse host tissue (H and I) in AD animals. MC1$^+$ neuronal cell bodies (arrowheads; K and N) and DNs around Congo red$^+$ Aβ deposits (pink, asterisks) (arrowheads; L and O) are found in human grafts and human Tau* grafts in AD mice, but not in mouse host tissue (Q and R). Arrowheads point to soma and DNs$^+$ structures. Asterisks mark Congo red$^+$ Aβ plaques. Counterstaining with hematoxylin (blue).

(S and T) Percentage of Aβ plaques surrounded by AT8$^+$ (S) and MC1$^+$ (T) DNs in human grafts (n = 4), human Tau* grafts (n = 3), and mouse host tissue (n = 3) in AD mice. Results are shown as mean ± SEM, one-way ANOVA with Kruskal-Wallis test, ****p < 0.0001; n.s., non-significant. Scale bars, 50 μm (A–R).

Transcriptome Analyses Reveal Human-Specific Signatures of AD

To assess global transcriptional changes in the human grafts in AD versus WT mice, we performed RNA-seq analysis at two time points: 4–5 MPT (young mice) and 8 MPT (old mice). Global analyses of gene expression patterns reveal interesting alterations in several gene ontology (GO) categories (Ashburner et al., 2000). Genes involved in synaptic transmission, gated channel activity, and neuron projection (GO:007268, GO:0022836, and GO:0043005) are significantly downregulated at 8 MPT in human neurons in AD versus WT mice (Figure 8A; Figure S8; Table S5). Additionally, genes involved in cognition and learning and memory (GO:0050890 and GO:0007611) also show a trend toward downregulation. GO categories related to immune or inflammatory response (GO:0002376 and GO:0006954) show a non-significant upregulation. It should be noted that our analysis includes only the human gene expression programs in the transplanted neurons and not the murine-derived immune cells of the brain (Figure 8A; Figure S8). Genes from the GO category regulation of cell death (GO:0010941) are upregulated at 8 MPT. Representative genes among these categories are shown in Figure 8B. Significant differential expression of mRNAs and non-coding RNAs is detected already at early, but more at late, stages in human transplants in AD versus WT mice (Tables S2–S5; for raw counts see Tables S6 and S7). Interestingly, among the most strongly upregulated genes in the human neurons in AD mice at 8 MPT (Table S4) are a couple of non-coding RNA genes: *LINC01007* and *RP11-89N17.4*. Genes involved in myelination (*MOBP*, *MAG*, *UGT8*, *MOG*, and *MBP*) are also upregulated in the transplanted human cells. Alterations in myelination are known to occur in AD (Ettle et al., 2016; Bartzokis, 2011), but few studies have investigated the role of oligodendrocytes and myelin in AD (De Strooper and Karran, 2016; Bartzokis, 2011). In the list of downregulated genes, we find *OTOF*, *GABRE*, *TAC1*, *PTK2B*, and *CACNA1H* involved in neurotransmission and *RHGAP36* involved in vesicle transport and regulation (Table S5). Interestingly *COL25A1*, also known as *CLAC*, is downregulated (Table S5). *CLAC* specifically binds to fibrillized Aβ and is present in Aβ plaques in AD patients (Hashimoto et al., 2002; Tong et al., 2010).

To further evaluate the relevance of our model for human AD, we compared the gene expression data from human neurons with a published dataset of human AD samples (Zhang et al., 2013). We performed co-expression clustering analysis using WCGNA (Langfelder and Horvath, 2008), yielding modules of genes showing a similar expression pattern across samples (Figure 8C). This analysis generated 37 modules from human transplants. The overlap of genes of these modules (left column) with the modules identified by Zhang et al. (2013) (right column) is determined using a Fisher's exact test. These data demonstrate that the transplanted human neurons show transcriptional changes in gene modules that are also affected in the human AD brain (Zhang et al., 2013).

DISCUSSION

The generation of better in vivo models that closely resemble the pathological features present in the human AD brain is instrumental to test new hypotheses with regard to AD etiology and for the validation of new therapeutic approaches. Ideally, such a model would incorporate a human genetic background, be versatile and robust, and include aspects such as innate inflammation, cellular heterogeneity, and minimal use of transgenes to drive the pathogenesis (De Strooper and Karran, 2016).

The main purpose of the current work was to ask to what extent a human/mouse brain chimera could be used to model critical aspects of AD previously uncovered by rodent models. We transplanted cortical neuronal precursors differentiated from one normal ESC line (H9) and from two FTD iPSC lines derived from the same patient into the brain of a well-characterized AD mouse model. Although three cell lines is a limited number, all displayed similar profound degeneration and necrosis when exposed to Aβ in a large number of independent transplantation experiments. In addition, the human-specific pathology was compared with host mouse neurons and transplanted PSC-derived murine neurons, which show much more resistance to Aβ pathology than the human neuronal counterparts.

At 4 MPT, already the human neurons show many signs of neurodegeneration. Dystrophic structures are found and presynaptic components, like synaptophysin and vesicular glutamate transporter 1, accumulate, while the dendritic marker MAP2 and the postsynaptic marker Homer1 disappear around Aβ plaques.

At 6 MPT, a significant loss of human neurons is found to an extent that has never been reported for mouse neurons in the many existing models for AD. Neuronal density is strongly reduced (down to 54%) in human grafts in AD versus WT mice whereas no significant differences were observed in mouse host tissue. Importantly, at 2 MPT, similar densities of human neurons are observed in AD and WT mice, indicating that integration is normal, and cell loss occurs only later over the course of the disease. EM analysis revealed that 33% of human neurons in AD mice show signs of degeneration at 6 MPT. The cell loss appears to be mostly necrotic based on morphological criteria. Genome-wide expression analysis of human transplants (8 MPT) shows, however, upregulation of a broader category of genes related to regulation of cell death. This GO category contains many genes that are only indirectly involved in the regulation of cell death processes. Further work will be needed to clarify whether some of the altered genes play causal roles in the cell death process that we observed here.

Strikingly, this major neurodegeneration and human neuronal loss occur in the absence of detectable tangle pathology. It was recently suggested that the induction of neuronal tangles critically depends on the expression of 4R Tau as seen in the human adult brain (Choi et al., 2014). At 2 and 4 MPT, the human neurons express mainly 3R isoforms, but after 6 MPT, 4R Tau isoforms are expressed in 89% of the human neurons. In addition, the 3R/4R Tau ratio in human neurons comes close to 1 at 8 MPT, as seen in the adult human brain, in contrast with most in vitro iPSC-derived models. We detect AT8 hyperphosphorylation and, notably, MC1 pathological conformational changes in Tau (Jicha et al., 1997) that are not detected in murine AD models. iPSCs expressing the Tau mutation Ex10+16 linked to FTD (Sposito et al., 2015) show an earlier appearance of 4R Tau and a higher tendency to cell death when exposed to Aβ.

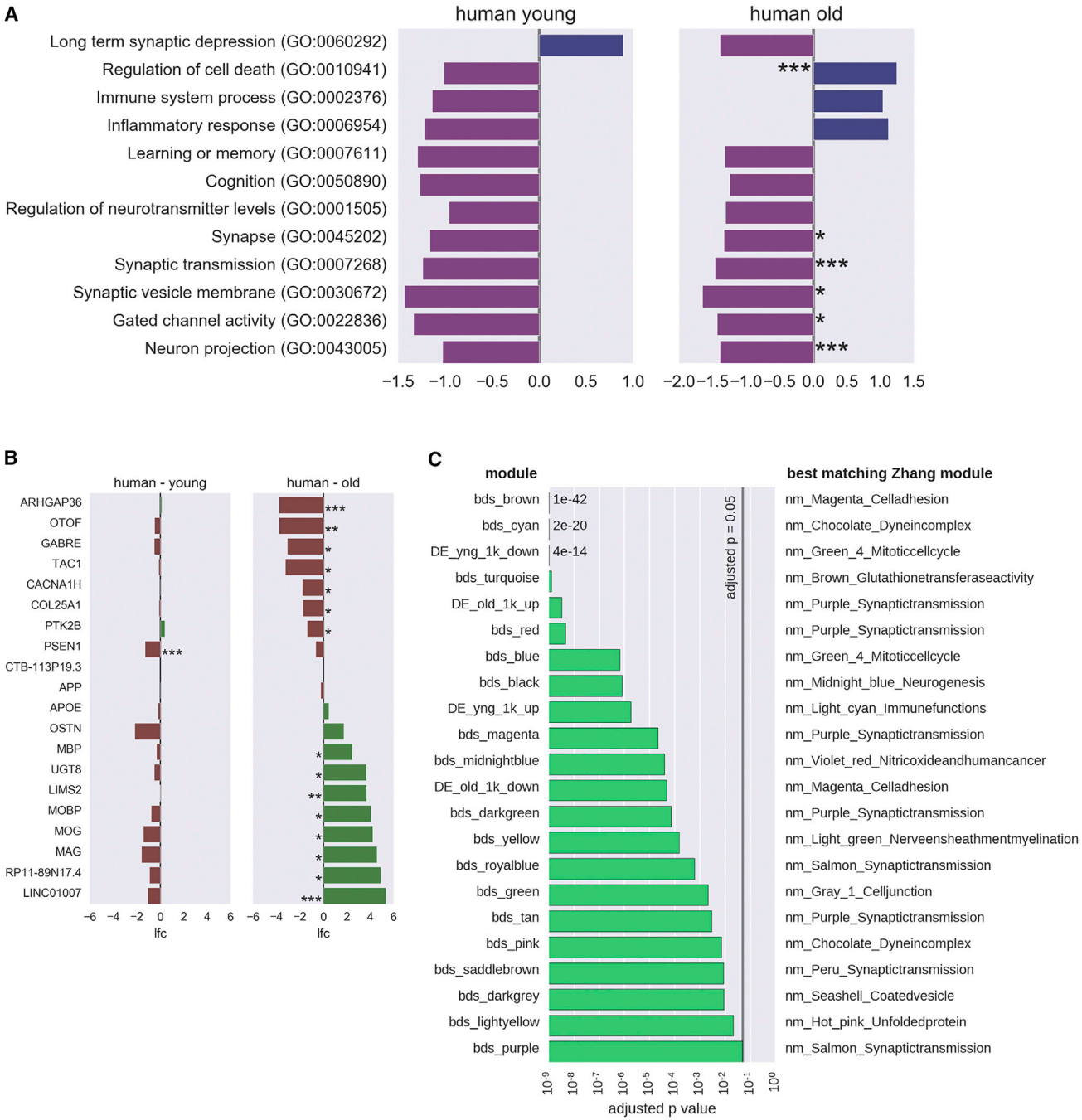

Figure 8. Transcriptional Changes in Human Neurons Grafted In Vivo

(A) Genes ranked according to the significance of the differential expression of upregulated (purple) and downregulated (blue) genes for young (4–5 MPT) and old (8 MPT) human grafts. The x axis shows the enrichment score according to the Gene Set Enrichment Analysis (GSEA). Significance of enrichment: ***$p < 0.001$; **$p < 0.01$; *$p < 0.05$.

(B) Log fold change of differential expression (brown: downregulation; green: upregulation) of a selected set of genes in young and old samples. p values are corrected for multiple testing: ***$p < 0.001$; **$p < 0.01$; *$p < 0.05$.

(C) WCGNA co-expression modules compared to the modules from Zhang et al. (2013). Four extra gene sets (prefix: DE) from the most differentially expressed genes (up and down in old and young mice) are included. Significance of overlap was determined by a Fisher's exact test and Benjamini-Hochberg multiple testing correction. The plot depicts the 22 modules (out of a total of 37) that show a significant overlap with the Zhang modules, indicating the best matching Zhang module on the right. The bars indicate the adjusted p value.

The data are in line with the idea that Tau expression is crucial for Aβ-induced toxicity in AD transgenic animals (Roberson et al., 2007; Leroy et al., 2012). However, we did not detect Tau tangles after 8 MPT in human neurons or in human Tau* neurons. Likely, even longer periods in vivo are required for detectable tangle pathology, or additional seeding is needed to induce the tangle conformation. The NOD-SCID background needed for the experiments unfortunately does not allow analysis beyond 8 MPT due to increased incidence of graft-unrelated tumor formation.

Recently, a three-dimensional in vitro AD model with human neuronal stem cells that overexpress mutated FAD genes was reported (Choi et al., 2014). This model uses matrigel as a 3D support matrix for the cells and recapitulates Aβ pathology. The model also presents pathological Tau phosphorylation and Tau filaments but fails to show neurodegeneration or cell death. We have not modified our neurons with APP or PSEN mutations, and neurons were grown within the brain, which is arguably a more natural situation than the matrigel used in the cell culture system. It is intriguing that Tau aggregation was detected in the cell culture system without neurodegeneration. Further investigations are needed to better understand the relationship, if any, between abnormal Tau conformation and cell death.

A particularly important aspect of the current approach is that innate immunity, believed to play an important role in AD (Heneka et al., 2015), remains apparently intact in the model. As shown, host-activated astrocytes and microglia cells are recruited to the human transplants, and similar neuroinflammatory responses are observed in human clusters and mouse host. Activated microglia cells have been proposed as essential for the cell loss in AD (Fuhrmann et al., 2010), and this might explain the lack of cell loss in the 3D cell culture system discussed above. In further experiments, it should be relevant to study how the loss of function of microglia cells in the host affects neurodegeneration in the human neurons in vivo (Fuhrmann et al., 2010).

Lastly, our model allows a genome-wide transcriptome analysis of the human neurons exposed to Aβ at early and late stages of the disease in vivo. Intriguingly, we observe two non-coding RNA sequences among the most upregulated genes. *RP11-89N17.4* expression might be altered in AD patients (Gui et al., 2015), and data from our lab show dysregulation of *LINC01007* in AD patients (data not shown). While these findings are still premature, it should motivate additional work exploring the role of non-coding RNAs in neurodegeneration (Salta and De Strooper, 2012). We also notice that *COL25A1* is downregulated at late stages. Interestingly, rare variants in *COL25A1* have been associated with healthy aging and possible protection against AD (Erikson et al., 2016). Other upregulated genes are involved in cell death and myelination, while many downregulated genes are implied in memory and cognition, synaptic transmission, gated channel activity, neurotransmitter levels, and neuron projection. We validated our model comparing our results with the results of a previous genome-wide gene expression study of AD patient brains (Zhang et al., 2013). The good concordance, taking into account that Zhang et al. (2013) provided data on total brain blocks from patients while we analyzed gene expression changes in human neurons specifically, is encouraging.

In conclusion, we present here a novel in vivo approach to investigate AD mechanisms in human neurons by generating a mouse/human brain chimera. This approach opens the door to explore how different human genetic backgrounds modulate AD-related features in vivo. The model is also of interest to further investigate whether and how Aβ modulates Tau pathology and how this affects neurodegeneration. This initial work demonstrates clearly the importance of a human molecular and cellular background to observe full neurodegeneration in the presence of Aβ plaques.

STAR★METHODS

Detailed methods are provided in the online version of this paper and include the following:

- KEY RESOURCES TABLE
- CONTACT FOR REAGENT AND RESOURCE SHARING
- EXPERIMENTAL MODEL AND SUBJECT DETAILS
  - Human and Mouse Pluripotent Stem Cells
  - AD and WT Immunodeficient Mice
  - AD Human Brain Samples
- METHOD DETAILS
  - Pluripotent Stem Cell Differentiation into Cortical Cells
  - Intracerebral Grafting
  - Immunofluorescence and Confocal Microscopy
  - Immunohistochemistry
  - Electron Microscopy and Immunogold
  - Aβ plaque Stainings
  - TUNEL Apoptosis Assay
  - Graft Dissection and RNA Extraction
  - RNA-seq Data Discrimination of Human Sequences in the Mixed Human + Mouse Sample
  - Cross-Mapping
  - Fraction of Reads Mapping
- QUANTIFICATION AND STATISTICAL ANALYSIS
  - Morphological Analysis for Quantification
  - Quantification of Aβ Plaque Burden
  - Quantification of Neuroinflammation
  - Quantifications of Ubiquitin+, SYP+, and VGlut1+ DNs
  - Quantification of Cell Density
  - Quantification of the Percentage of 4R Tau+ Cells
  - Quantification of the Percentage of Aβ Plaques Surrounded by AT8 or $MC1^{+}$ DNs
  - RNA-Seq Data Analysis
  - Differential Expression Analysis
  - Enrichment Analysis
  - Determination of Tau Splice Form Usage
- DATA AND SOFTWARE AVAILABILITY

SUPPLEMENTAL INFORMATION

Supplemental Information includes eight figures and seven tables and can be found with this article online at http://dx.doi.org/10.1016/j.neuron.2017.02.001.

AUTHOR CONTRIBUTIONS

I.E.-C., A.M.A., I.T., P.V., and B.D.S. conceived the study and planned experiments. I.E.-C. and A.M.A. performed the experiments with the help of M.F., A.S., K.A., S.M., J.B., L.L., N.C., L.O., E.V.E., E.R., S.W., A.E., J.H., K.L., and

J.-P.B. All authors interpreted data. I.E.-C., A.M.A., P.V., and B.D.S. wrote the first version of the manuscript. All authors contributed to and approved the final version. RNA-seq data analysis was performed by M.F.

ACKNOWLEDGMENTS

This work was supported by the European Research Council ERC-2010-AG_268675 to B.D.S., the Fonds voor Wetenschappelijk Onderzoek (FWO), the KU Leuven and VIB, and a Methusalem grant from the KU Leuven/Flemish Government to B.D.S. B.D.S. is supported by the Bax-Vanluffelen Chair for Alzheimer's Disease and "Opening the Future" of the Leuven Universiteit Fonds (LUF). This work is supported by Vlaams Initiatief voor Netwerken voor Dementie Onderzoek (VIND, Strategic Basic Research Grant 135043). P.V. is supported by the Belgian Queen Elizabeth Medical Foundation, the WELBIO Program of the Walloon Region, the Fondation de SPOELBERCH, the AXA Research Fund, the Fondation ULB, and ERC-2013 ERC-2013-AG_340020. Confocal microscope equipment was acquired through a Hercules Type 1 AKUL/09/037 to W. Annaert. Confocal and electron microscopy were performed in the VIB Bio Imaging Core (LiMoNe and EMoNe facilities). Mouse experiments were supported by Inframouse (KU Leuven and VIB). J.-P.B. was supported by grants from the Belgian Fonds de la Recherche Scientifique Médicale (T.0023.15), the Fund Aline (King Baudoin Foundation and Foundation for Alzheimer Research [FRA/SAO] [S#14001]), and the Fund Génicot (ULB - 2015). K.A. is a research fellow of the Belgian Fonds National de la Recherche Scientifique (F.N.R.S.) (and supported by grant 1.B.007.15). This work was supported by the IAP program (P7/16 and P7/20) of the Belgian Federal Science Policy Office. S.W. and J.H. received funding from the NIHR Queen Square Dementia Biomedical Research Unit.

We thank Prof. Luc Buee and Prof. Raphaelle Caillierez for the human AD brain samples and Prof. Colin Mahoney and Prof. Nick Fox for the human iPSC collection. We thank Veronique Hendrickx and Jonas Verwaeren for help with the mouse colonies and Dr. Annerieke Sierksma and Dr. Evgenia Salta for help with statistics and gene information.

B.D.S. is a consultant for Janssen Pharmaceutics and Remynd NV. He receives research funding from Janssen Pharmaceutics.

Received: March 21, 2016
Revised: December 12, 2016
Accepted: January 31, 2017
Published: February 23, 2017

REFERENCES

Alzheimer, A. (1906). Über einen eigenartigen schweren Erkrankungsprozeβ der Hirnrinde. Neurol. Central *25*, 1134.

Arranz, A.M., Gottlieb, M., Pérez-Cerdá, F., and Matute, C. (2010). Increased expression of glutamate transporters in subcortical white matter after transient focal cerebral ischemia. Neurobiol. Dis. *37*, 156–165.

Arranz, A.M., Delbroek, L., Van Kolen, K., Guimarães, M.R., Mandemakers, W., Daneels, G., Matta, S., Calafate, S., Shaban, H., Baatsen, P., et al. (2015). LRRK2 functions in synaptic vesicle endocytosis through a kinase-dependent mechanism. J. Cell Sci. *128*, 541–552.

Ashburner, M., Ball, C.A., Blake, J.A., Botstein, D., Butler, H., Cherry, J.M., Davis, A.P., Dolinski, K., Dwight, S.S., Eppig, J.T., et al.; The Gene Ontology Consortium (2000). Gene ontology: tool for the unification of biology. Nat. Genet. *25*, 25–29.

Ashe, K.H., and Zahs, K.R. (2010). Probing the biology of Alzheimer's disease in mice. Neuron *66*, 631–645.

Bartzokis, G. (2011). Alzheimer's disease as homeostatic responses to age-related myelin breakdown. Neurobiol. Aging *32*, 1341–1371.

Benjamini, Y., and Hochberg, Y. (1995). Controlling the false discovery rate: a practical and powerful approach to multiple testing. J. R. Stat. Soc. B *57*, 289–300.

Brennand, K.J., Marchetto, M.C., Benvenisty, N., Brüstle, O., Ebert, A., Izpisua Belmonte, J.C., Kaykas, A., Lancaster, M.A., Livesey, F.J., McConnell, M.J., et al. (2015). Creating patient-specific neural cells for the in vitro study of brain disorders. Stem Cell Reports *5*, 933–945.

Brion, J.P., Couck, A.M., Bruce, M., Anderton, B., and Flament-Durand, J. (1991). Synaptophysin and chromogranin A immunoreactivities in senile plaques of Alzheimer's disease. Brain Res. *539*, 143–150.

Burattini, S., and Falcieri, E. (2013). Analysis of cell death by electron microscopy. Methods Mol. Biol. *1004*, 77–89.

Choi, S.H., Kim, Y.H., Hebisch, M., Sliwinski, C., Lee, S., D'Avanzo, C., Chen, H., Hooli, B., Asselin, C., Muffat, J., et al. (2014). A three-dimensional human neural cell culture model of Alzheimer's disease. Nature *515*, 274–278.

Crews, L., and Masliah, E. (2010). Molecular mechanisms of neurodegeneration in Alzheimer's disease. Hum. Mol. Genet. *19* (R1), R12–R20.

De Strooper, B., and Karran, E. (2016). The cellular phase of Alzheimer's disease. Cell *164*, 603–615.

Dobin, A., Davis, C.A., Schlesinger, F., Drenkow, J., Zaleski, C., Jha, S., Batut, P., Chaisson, M., and Gingeras, T.R. (2013). STAR: ultrafast universal RNA-seq aligner. Bioinformatics *29*, 15–21.

Dolmetsch, R., and Geschwind, D.H. (2011). The human brain in a dish: the promise of iPSC-derived neurons. Cell *145*, 831–834.

Erikson, G.A., Bodian, D.L., Rueda, M., Molparia, B., Scott, E.R., Scott-Van Zeeland, A.A., Topol, S.E., Wineinger, N.E., Niederhuber, J.E., Topol, E.J., and Torkamani, A. (2016). Whole-genome sequencing of a healthy aging cohort. Cell *165*, 1002–1011.

Espuny-Camacho, I., Michelsen, K.A., Gall, D., Linaro, D., Hasche, A., Bonnefont, J., Bali, C., Orduz, D., Bilheu, A., Herpoel, A., et al. (2013). Pyramidal neurons derived from human pluripotent stem cells integrate efficiently into mouse brain circuits in vivo. Neuron *77*, 440–456.

Ettle, B., Schlachetzki, J.C., and Winkler, J. (2016). Oligodendroglia and myelin in neurodegenerative disorders: more than just bystanders? Mol. Neurobiol. *53*, 3046–3062.

Fuhrmann, M., Bittner, T., Jung, C.K.E., Burgold, S., Page, R.M., Mitteregger, G., Haass, C., LaFerla, F.M., Kretzschmar, H., and Herms, J. (2010). Microglial Cx3cr1 knockout prevents neuron loss in a mouse model of Alzheimer's disease. Nat. Neurosci. *13*, 411–413.

Gaspard, N., Bouschet, T., Hourez, R., Dimidschstein, J., Naeije, G., van den Ameele, J., Espuny-Camacho, I., Herpoel, A., Passante, L., Schiffmann, S.N., et al. (2008). An intrinsic mechanism of corticogenesis from embryonic stem cells. Nature *455*, 351–357.

Goedert, M., and Jakes, R. (1990). Expression of separate isoforms of human tau protein: correlation with the tau pattern in brain and effects on tubulin polymerization. EMBO J. *9*, 4225–4230.

Gui, Y., Liu, H., Zhang, L., Lv, W., and Hu, X. (2015). Altered microRNA profiles in cerebrospinal fluid exosome in Parkinson disease and Alzheimer disease. Oncotarget *6*, 37043–37053.

Hardy, J., and Selkoe, D.J. (2002). The amyloid hypothesis of Alzheimer's disease: progress and problems on the road to therapeutics. Science *297*, 353–356.

Hashimoto, T., Wakabayashi, T., Watanabe, A., Kowa, H., Hosoda, R., Nakamura, A., Kanazawa, I., Arai, T., Takio, K., Mann, D.M.A., and Iwatsubo, T. (2002). CLAC: a novel Alzheimer amyloid plaque component derived from a transmembrane precursor, CLAC-P/collagen type XXV. EMBO J. *21*, 1524–1534.

Heneka, M.T., Golenbock, D.T., and Latz, E. (2015). Innate immunity in Alzheimer's disease. Nat. Immunol. *16*, 229–236.

Hu, W., Qiu, B., Guan, W., Wang, Q., Wang, M., Li, W., Gao, L., Shen, L., Huang, Y., Xie, G., et al. (2015). Direct conversion of normal and Alzheimer's disease human fibroblasts into neuronal cells by small molecules. Cell Stem Cell *17*, 204–212.

Hutton, M., Lendon, C.L., Rizzu, P., Baker, M., Froelich, S., Houlden, H., Pickering-Brown, S., Chakraverty, S., Isaacs, A., Grover, A., et al. (1998). Association of missense and 5′-splice-site mutations in tau with the inherited dementia FTDP-17. Nature *393*, 702–705.

Israel, M.A., Yuan, S.H., Bardy, C., Reyna, S.M., Mu, Y., Herrera, C., Hefferan, M.P., Van Gorp, S., Nazor, K.L., Boscolo, F.S., et al. (2012). Probing sporadic and familial Alzheimer's disease using induced pluripotent stem cells. Nature *482*, 216–220.

Jicha, G.A., Bowser, R., Kazam, I.G., and Davies, P. (1997). Alz-50 and MC-1, a new monoclonal antibody raised to paired helical filaments, recognize conformational epitopes on recombinant tau. J. Neurosci. Res. *48*, 128–132.

Katzman, R. (1986). Alzheimer's disease. N. Engl. J. Med. *314*, 964–973.

Kokjohn, T.A., and Roher, A.E. (2009). Amyloid precursor protein transgenic mouse models and Alzheimer's disease: understanding the paradigms, limitations, and contributions. Alzheimers Dement. *5*, 340–347.

Kondo, T., Asai, M., Tsukita, K., Kutoku, Y., Ohsawa, Y., Sunada, Y., Imamura, K., Egawa, N., Yahata, N., Okita, K., et al. (2013). Modeling Alzheimer's disease with iPSCs reveals stress phenotypes associated with intracellular Aβ and differential drug responsiveness. Cell Stem Cell *12*, 487–496.

LaFerla, F.M., and Green, K.N. (2012). Animal models of Alzheimer disease. Cold Spring Harb. Perspect. Med. *2*, 2.

Langfelder, P., and Horvath, S. (2008). WGCNA: an R package for weighted correlation network analysis. BMC Bioinformatics *9*, 559.

Leroy, K., Ando, K., Laporte, V., Dedecker, R., Suain, V., Authelet, M., Héraud, C., Pierrot, N., Yilmaz, Z., Octave, J.N., and Brion, J.P. (2012). Lack of tau proteins rescues neuronal cell death and decreases amyloidogenic processing of APP in APP/PS1 mice. Am. J. Pathol. *181*, 1928–1940.

Liao, Y., Smyth, G.K., and Shi, W. (2014). featureCounts: an efficient general purpose program for assigning sequence reads to genomic features. Bioinformatics *30*, 923–930.

McGeer, P.L., Itagaki, S., Tago, H., and McGeer, E.G. (1988). Occurrence of HLA-DR reactive microglia in Alzheimer's disease. Ann. N Y Acad. Sci. *540*, 319–323.

Michelsen, K.A., Acosta-Verdugo, S., Benoit-Marand, M., Espuny-Camacho, I., Gaspard, N., Saha, B., Gaillard, A., and Vanderhaeghen, P. (2015). Area-specific reestablishment of damaged circuits in the adult cerebral cortex by cortical neurons derived from mouse embryonic stem cells. Neuron *85*, 982–997.

Morrissette, D.A., Parachikova, A., Green, K.N., and LaFerla, F.M. (2009). Relevance of transgenic mouse models to human Alzheimer disease. J. Biol. Chem. *284*, 6033–6037.

Muratore, C.R., Rice, H.C., Srikanth, P., Callahan, D.G., Shin, T., Benjamin, L.N., Walsh, D.M., Selkoe, D.J., and Young-Pearse, T.L. (2014). The familial Alzheimer's disease APPV717I mutation alters APP processing and Tau expression in iPSC-derived neurons. Hum. Mol. Genet. *23*, 3523–3536.

Nagańska, E., and Matyja, E. (2001). Ultrastructural characteristics of necrotic and apoptotic mode of neuronal cell death in a model of anoxia in vitro. Folia Neuropathol. *39*, 129–139.

Paşca, S.P., Panagiotakos, G., and Dolmetsch, R.E. (2014). Generating human neurons in vitro and using them to understand neuropsychiatric disease. Annu. Rev. Neurosci. *37*, 479–501.

Radde, R., Bolmont, T., Kaeser, S.A., Coomaraswamy, J., Lindau, D., Stoltze, L., Calhoun, M.E., Jäggi, F., Wolburg, H., Gengler, S., et al. (2006). Abeta42-driven cerebral amyloidosis in transgenic mice reveals early and robust pathology. EMBO Rep. *7*, 940–946.

Ritchie, M.E., Phipson, B., Wu, D., Hu, Y., Law, C.W., Shi, W., and Smyth, G.K. (2015). limma powers differential expression analyses for RNA-sequencing and microarray studies. Nucleic Acids Res. *43*, e47.

Roberson, E.D., Scearce-Levie, K., Palop, J.J., Yan, F., Cheng, I.H., Wu, T., Gerstein, H., Yu, G.Q., and Mucke, L. (2007). Reducing endogenous tau ameliorates amyloid beta-induced deficits in an Alzheimer's disease mouse model. Science *316*, 750–754.

Robinson, M.D., McCarthy, D.J., and Smyth, G.K. (2010). edgeR: a Bioconductor package for differential expression analysis of digital gene expression data. Bioinformatics *26*, 139–140.

Sagare, A.P., Bell, R.D., Zhao, Z., Ma, Q., Winkler, E.A., Ramanathan, A., and Zlokovic, B.V. (2013). Pericyte loss influences Alzheimer-like neurodegeneration in mice. Nat. Commun. *4*, 2932.

Salta, E., and De Strooper, B. (2012). Non-coding RNAs with essential roles in neurodegenerative disorders. Lancet Neurol. *11*, 189–200.

Shi, Y., Kirwan, P., Smith, J., MacLean, G., Orkin, S.H., and Livesey, F.J. (2012). A human stem cell model of early Alzheimer's disease pathology in Down syndrome. Sci. Transl. Med. *4*, 124ra29.

Shultz, L.D., Schweitzer, P.A., Christianson, S.W., Gott, B., Schweitzer, I.B., Tennent, B., McKenna, S., Mobraaten, L., Rajan, T.V., Greiner, D.L., et al. (1995). Multiple defects in innate and adaptive immunologic function in NOD/LtSz-scid mice. J. Immunol. *154*, 180–191.

Spillantini, M.G., and Goedert, M. (2013). Tau pathology and neurodegeneration. Lancet Neurol. *12*, 609–622.

Sposito, T., Preza, E., Mahoney, C.J., Setó-Salvia, N., Ryan, N.S., Morris, H.R., Arber, C., Devine, M.J., Houlden, H., Warner, T.T., et al. (2015). Developmental regulation of tau splicing is disrupted in stem cell-derived neurons from frontotemporal dementia patients with the 10 + 16 splice-site mutation in MAPT. Hum. Mol. Genet. *24*, 5260–5269.

Suzuki, I.K., and Vanderhaeghen, P. (2015). Is this a brain which I see before me? Modeling human neural development with pluripotent stem cells. Development *142*, 3138–3150.

Thomson, J.A., Itskovitz-Eldor, J., Shapiro, S.S., Waknitz, M.A., Swiergiel, J.J., Marshall, V.S., and Jones, J.M. (1998). Embryonic Stem Cell Lines Derived from Human Blastocysts. Science *282*, 1145–1147.

Tong, Y., Xu, Y., Scearce-Levie, K., Ptácek, L.J., and Fu, Y.H. (2010). COL25A1 triggers and promotes Alzheimer's disease-like pathology in vivo. Neurogenetics *11*, 41–52.

Ueda, H., Fujita, R., Yoshida, A., Matsunaga, H., and Ueda, M. (2007). Identification of prothymosin-alpha1, the necrosis-apoptosis switch molecule in cortical neuronal cultures. J. Cell Biol. *176*, 853–862.

van den Ameele, J., Tiberi, L., Vanderhaeghen, P., and Espuny-Camacho, I. (2014). Thinking out of the dish: what to learn about cortical development using pluripotent stem cells. Trends Neurosci. *37*, 334–342.

Vera, E., and Studer, L. (2015). When rejuvenation is a problem: challenges of modeling late-onset neurodegenerative disease. Development *142*, 3085–3089.

Weaver, C.L., Espinoza, M., Kress, Y., and Davies, P. (2000). Conformational change as one of the earliest alterations of tau in Alzheimer's disease. Neurobiol. Aging *21*, 719–727.

Yagi, T., Ito, D., Okada, Y., Akamatsu, W., Nihei, Y., Yoshizaki, T., Yamanaka, S., Okano, H., and Suzuki, N. (2011). Modeling familial Alzheimer's disease with induced pluripotent stem cells. Hum. Mol. Genet. *20*, 4530–4539.

Zhang, B., Gaiteri, C., Bodea, L.G., Wang, Z., McElwee, J., Podtelezhnikov, A.A., Zhang, C., Xie, T., Tran, L., Dobrin, R., et al. (2013). Integrated systems approach identifies genetic nodes and networks in late-onset Alzheimer's disease. Cell *153*, 707–720.

STAR★METHODS

KEY RESOURCES TABLE

REAGENT or RESOURCE	SOURCE	IDENTIFIER
Antibodies		
3R Tau	Millipore	Cat# 05-803 RRID: AB_310013
4R Tau	Millipore	Cat# 05-804 RRID: AB_310014
6E10	Covance Research Products	Cat# SIG-39320-1000 RRID: AB_10175145
AT8	Thermo Fisher Scientific	Cat# MN1020 RRID: AB_223647
B3Tubb	Covance Research Products	Cat# PRB-435P-100 RRID: AB_291637
B3Tubb	Covance Research Products	Cat# MMS-435P RRID: AB_2313773
B3Tubb	Millipore	Cat# AB9354 RRID: AB_570918
Brn2	Santa Cruz Biotechnology	Cat# sc-6029 RRID: AB_2167385
CTIP2	Abcam	Cat# ab18465 RRID: AB_2064130
Foxg1	Abcam	Cat# ab18259 RRID: AB_732415
GFAP	Dako	Cat# Z0334 RRID: AB_10013382
GFAP	Synaptic Systems	Cat# 173 004 RRID: AB_10641162
GFP	Abcam	Cat# ab13970 RRID: AB_300798
GFP	Thermo Fisher Scientific	Cat# A-6455 RRID: AB_221570
Human NCAM	Santa Cruz Biotechnology	Cat# sc-106 RRID: AB_627128
Human NCAM	Abcam	Cat# ab75813 RRID: AB_2632384
Human Nuclear Antigen	Millipore	Cat# MAB1281 RRID: AB_94090
Homer 1	Synaptic Systems	Cat# 160 003 RRID: AB_887730
Iba1	Wako	Cat# 019-19741 RRID: AB_839504
MAP2	Sigma-Aldrich	Cat# M9942 RRID: AB_477256
MAP2	Santa Cruz Biotechnology	Cat# sc-20172 RRID: AB_2250101
MC1	Gift from P. Davis	N/A
NeuN	Millipore	Cat# MAB377 RRID: AB_2298772
PSD95	BD Biosciences	Cat# 610495 RRID: AB_397861
Satb2	Abcam	Cat# ab34735 RRID: AB_2301417
STEM121	Stem Cells	Cat# AB-121-U-050 RRID: AB_2632385
SYP	Synaptic Systems	Cat# 101 011 RRID: AB_887824
SYP	Synaptic Systems	Cat# 101 002 RRID: AB_887905
Tau	Dako	Cat# A0024 RRID: AB_10013724
Tbr1	Abcam	Cat# ab31940 RRID: AB_2200219
Ubiquitin	Dako	Cat# Z0458 RRID: AB_2315524
VGlut1	Synaptic Systems	Cat# 135 303 RRID: AB_887875
Anti-mouse 488	Thermo Fisher Scientific	Cat# A-11001 RRID: AB_2534069
Anti-mouse 546	Thermo Fisher Scientific	Cat# A-11030 RRID: AB_2534089
Anti-mouse 594	Thermo Fisher Scientific	Cat# A-11005 RRID: AB_2534073
Anti-mouse 650	Thermo Fisher Scientific	Cat# 84545 RRID: AB_10942301
Anti-mouse 680	Rockland	Cat# 610-144-121 RRID: AB_1057546
Anti-mouse biotinylated	Vector Laboratories	Cat# BA-9200 RRID: AB_2336171
Anti-mouse biotinylated	Vector Laboratories	Cat# BA-2000 RRID: AB_2313571
Anti-mouse Ultrasmall 0.8 nm IgG	Aurion	Cat# 800.022 RRID: AB_2632382
Anti-rabbit 488	Thermo Fisher Scientific	Cat# A-11034, also A11034 RRID: AB_2576217
Anti-rabbit 594	Thermo Fisher Scientific	Cat# A21207 RRID: AB_141637

(*Continued on next page*)

Continued

REAGENT or RESOURCE	SOURCE	IDENTIFIER
Anti-rabbit 568	Thermo Fisher Scientific	Cat# A-11011, also A11011 RRID: AB_143157
Anti-rabbit 647	Thermo Fisher Scientific	Cat# A-21245, also A21245 RRID: AB_2535813
Anti-rabbit biotinylated	Vector Laboratories	Cat# BA-1000 RRID: AB_2313606
Anti-rabbit Ultrasmall 0.8 nm IgG	Aurion	Cat# 800.011 RRID: AB_2632383
Anti-chicken 488	Thermo Fisher Scientific	Cat# A-11039 RRID: AB_2534096
Anti-chicken 555	Thermo Fisher Scientific	Cat# A-21437 RRID: AB_2535858
Anti-chicken 647	Thermo Fisher Scientific	Cat# A-21449 RRID: AB_2535866
Anti-guinea pig 647	Jackson ImmunoResearch Laboratories	Cat# 106-605-003 RRID: AB_2337446
Biological Samples		
Human AD brain samples	Brion, J.P., ULB, Brussels Buee, L., and Caillierez R.,, University of Lille, France	N/A
Chemicals, Peptides, and Recombinant Proteins		
ROCK inhibitor	Calbiochem	Cat# Y-27632
Noggin	R&D Systems	Cat# 1967-NG-025
Critical Commercial Assays		
Apop Tag Plus in situ apoptosis fluorescein detection kit	Chemicon/Millipore	Cat# S7111
Silver enhancement kit HQ Silver	Nanoprobes	Cat# 2012
Deposited Data		
RNA-seq raw featurecounts from human PSC-derived neurons grafted into the cortex of AD and WT mice	This paper	Table S6
RNA-seq raw featurecounts from murine AD and WT cortex	This paper	Table S7
Experimental Models: Cell Lines		
Human ESC H9 line stably transduced with GFP	H9 (WA09) original line (Thomson et al., 1998) WiCell Research Institute H9-GFP line was generated by Espuny-Camacho et al., 2013 ULB, Brussels	H9-GFP
Mouse ESC E14 line stably transduced with GFP	E14 original line obtained from Baygenomics E14-GFP line was generated by Gaspard et al., 2008, ULB, Brussels	E14-GFP
Human Tau Ex10+16 mutation (Tau*) line 11028V97	Wray, S. and Hardy, J., UCL, London	11028V97
Human Tau Ex10+16 mutation (Tau*) line 11028V98	Wray, S. and Hardy, J., UCL, London	11028V98
Experimental Models: Organisms/Strains		
(WT mice) APP PS1 wt/wt Prkdc $^{scid/scid}$	This paper	Prkdc $^{scid/scid}$, The Jackson Laboratory, Shultz et al., 1995, RRID: IMSR_JAX:001303; APP PS1 wt/wt, Radde et al., 2006, RRID: MGI:5313530
(AD mice) APP PS1 tg/wt Prkdc $^{scid/scid}$	This paper	Prkdc $^{scid/scid}$, The Jackson Laboratory, Shultz et al., 1995, RRID: IMSR_JAX:001303; APP PS1 tg/wt, Radde et al., 2006, RRID: MGI:5313530
Software and Algorithms		
STAR RNA-seq aligner	Dobin et al., 2013	https://github.com/alexdobin/STAR
Subread/Featurecounts	Liao et al., 2014	http://subread.sourceforge.net/
Pandas Python Data Analysis Library	N/A	http://pandas.pydata.org/

(*Continued on next page*)

Continued

REAGENT or RESOURCE	SOURCE	IDENTIFIER
Limma/Linear Models for Microarray Data	Ritchie et al., 2015	https://bioconductor.org/packages/release/bioc/html/limma.html
Benjamini-Hochberg algorithm	Benjamini and Hochberg, 1995	

CONTACT FOR REAGENT AND RESOURCE SHARING

Further information and requests for resources and reagents should be directed to and will be fulfilled by the Lead Contact Prof. Bart De Strooper (bart.destrooper@vib.be).

EXPERIMENTAL MODEL AND SUBJECT DETAILS

Human and Mouse Pluripotent Stem Cells

Experiments were performed using the H9 line stably expressing GFP under the control of chicken β-actin promoter (H9-GFP line) generated previously (Espuny-Camacho et al., 2013), 2 iPSC lines carrying the Tau Ex10+16 mutation derived from one FTD patient (Sposito et al., 2015) and the mouse E14 line stably expressing GFP under the control of the chicken β-actin promoter (E14-GFP line) generated previously (Gaspard et al., 2008). Human and mouse pluripotent stem cells (PSC) lines were cultured and passaged on mitotically inactivated mouse embryonic fibroblasts (MEFs) (Espuny-Camacho et al., 2013).

Karyotyping and CGH Array

The karyotyping of the iPSC Tau Ex10+16 lines was analyzed by Cell Guidance Systems (UK). For the CGH array analysis of the ESC H9-GFP line, the genomic DNA was extracted using the QIAamp DNA Blood Mini QIAcube Kit on the Qiacube robotic workstation according to the manufacturer's instructions. Array analysis was performed using the 8x 60K CytoSure ISCA v2 microarray (AMADID 020040, Oxford Gene Technology, OGT, Oxford, UK). Genomic DNA was labeled for 2 hr using the CytoSure Labeling Kit (Oxford Gene Technology). The sample was labeled with Cy5 and hybridized versus Cy3-labeled sex-matched reference DNA. Hybridization was performed for minimum 16 hr in a rotator oven (SciGene, CA, USA) at 65°C. Washing of arrays was performed using Agilent wash solutions with a Little Dipper Microarray Processor (SciGene). Arrays were scanned using an Agilent microarray scanner at 2 μm resolution, followed by calculation of signal intensities using Feature Extraction software (Agilent Technologies). Visualization of results and data analysis was performed using the CytoSure Interpret Software (Oxford Gene Technology) and the circular binary segmentation algorithm. Quality control metrics are monitored with CytoSure Interpret software (Oxford Gene Technology).

AD and WT Immunodeficient Mice

APP PS1 tg/wt mice (expressing KM670/671NL mutated APP and L166P mutated PS1 under the control of the Thy1.2 promoter1.1) (Radde et al., 2006) were crossed with the immunodeficient NOD-SCID mice (NOD.CB17-*Prkdc*^{scid}) that carry a single point mutation in the *Prkdc* gene (Shultz et al., 1995). APP PS1 tg/wt *Prkdc*$^{scid/+}$ mice from the F1 generation were crossed with NOD-SCID mice to generate APP PS1tg/wt *Prkdc*$^{scid/scid}$ immunodeficient mice. APP PS1 tg/wt *Prkdc*$^{scid/scid}$ mice were subsequently crossed with NOD-SCID mice to generate either APP PS1 tg/wt *Prkdc*$^{scid/scid}$ (AD mice) or APP PS1 wt/wt *Prkdc*$^{scid/scid}$ (WT mice) used for transplantations. Mice were housed in IVC cages in a SPF facility; light/dark cycle and temperature were always monitored. After weaning, no more than 4 animals of the same gender were kept per cage.

The APP and PS1 genotyping was done as previously described (Radde et al., 2006). The Prkdc genotyping was done by PCR amplification using the primers: Forward 5′ GGA AAA GAA TTG GTA TCC AC 3′; Reverse 5′ AGT TAT AAC AGC TGG GTT GGC 3′; followed by restriction digestion analysis of the amplicon with AluI enzyme (Roche Diagnostics). Products were analyzed on a 3% agarose gel.

Transplantation experiments were performed in both male and female littermates at P0. The total number of animals used for transplantation and further analyses is indicated in Table S1. Mouse work was performed in accordance with institutional and national guidelines and regulations, and following approval of the Ethical Committee of the KUL. All experiments conform to the relevant regulatory standards.

AD Human Brain Samples

Left hemisphere from 3 demented patients (patient 1: female, 60 years; patient 2: male, 65 years; patient 3: female, 70 years) clinically diagnosed as AD were taken at autopsy and fixed with formalin 10%. Tissue samples from several brain areas were further dissected and embedded in paraffin for microscopic examination. The neuropathological analysis confirmed the presence of numerous neurofibrillary tangles and senile plaques (Braak stage V-VI for neurofibrillary tangles, Thal stage 4 to 5 for Aβ amyloid). Samples from the frontal cortex and from the anterior hippocampus (approximately 3x3x1 cm) were cut in 10 μm thick coronal sections and used for immunohistochemical analysis (Figures S3 and S7).

This study on post-mortem brain tissue was performed in compliance and following approval of the Ethical Committee of the Medical School of the Free University of Brussels.

METHOD DETAILS

Pluripotent Stem Cell Differentiation into Cortical Cells

Human and mouse PSC cells were differentiated into cortical progenitors and neurons in vitro as previously described (Espuny-Camacho et al., 2013). Briefly cells were dissociated manually or enzymatically using Stem-Pro Accutase on day-2, (Invitrogen A11105) and plated on matrigel (BD, hES qualified matrigel) coated-coverslips/dishes at low confluency (5,000–10,000 cells/cm2) in MEF-conditioned hES/hiPS medium supplemented with ROCK inhibitor (Y-27632; 10 μM Calbiochem, 688000). On day 0 of the differentiation, the medium was changed to DDM supplemented with B27 (10 mL B27 per 500 mL DDM, GIBCO) and Noggin (100 ng/ml, R&D Systems) and the medium was replenished every 2 days. After 16 DIV, the medium was changed to DDM supplemented with B27 (GIBCO) and changed every 2 days. The cultures used for the experiments were routinely monitored for normal progenitor cell proliferation and rosette radial glia formation in culture under phase-contrast microscope analysis. Cultures that underwent normal parameters were used for transplantation experiments. At 14 DIV (for mouse PSC) and 24 DIV (for human PSC), the progenitors were manually or enzymatically (Stem-Pro Accutase) dissociated and injected into newborn mice recipients. Some cultures were kept in vitro after dissociation for cell identity analysis, resuspended in DDM supplemented with B27 and ROCK inhibitor (10 μM) and plated onto poly-Lysin/Laminin coated coverslips. 5-7 days after dissociation, half of the medium was replenished with Neurobasal supplemented with B27 (10 mL B27 per 500 mL DDM) and 2mM glutamine, and changed again every 5-7 days.

Intracerebral Grafting

Grafting experiments of human and mouse PSC-derived cortical progenitors and neurons were performed as previously described (Gaspard et al., 2008; Espuny-Camacho et al., 2013) using the APP PS1 tg/wt NOD-SCID (AD mice) and APP PS1 wt/wt NOD-SCID (WT mice) at P0. Briefly, human and mouse PSC-derived cortical progenitors and neurons were manually or enzymatically dissociated, supplemented with ROCK inhibitor (Y-27632; 10 μM Calbiochem, 688000) and injected into the frontal cortex of AD or WT mice. Around 100.000 cells were injected in suspension. The total number of animals used for transplantation and further analyses is indicated in Table S1.

Immunofluorescence and Confocal Microscopy

For IF analysis, mice were anesthetized with CO2 and perfused with phosphate-buffered saline followed by 4% paraformaldehyde solution. The brain was then removed; post-fixed in the same fixative over 48-72 hr and cut into 60 μm slices on a Leica VT1000S vibratome. IF on grafted brains was performed as described previously (Arranz et al., 2010; Espuny-Camacho et al., 2013) using primary and secondary antibodies (see Key Resources Table). Antigen retrieval was performed by microwave boiling the slides in 10 mM tri-Sodium Citrate buffer pH 6.0 (VWR). Nuclei staining was performed using a specific anti-human nuclei antibody (HuNuclei) (see Key Resources Table), the pan-nuclear staining TOPRO3 (Invitrogen), or DAPI (SIGMA). Confocal Images were obtained using a Nikon Ti-E inverted microscope equipped with an A1R confocal unit driven by NIS (4.30) software. The confocal was outfitted with 20x (0.75 NA), 40x oil (1.4 NA) and 60x oil (1.4 NA) objectives lenses. For excitation 405 nm, 488 nm, 561 nm, 638 nm laser lines were used.

Immunohistochemistry

Mice were anesthetized with CO_2, decapitated, and their brains were dissected and immersed in 10% (v/v) formalin for 24 hr. Brains were embedded in paraffin, cut on a Microm HM360 sliding microtome at 6 μm and mounted. Sections were deparaffinized in xylene, serially transferred to 100%, 90%, 70%, 50% ethanol solutions and rinsed. IHC was performed modifying the procedures described previously (Arranz et al., 2010; Espuny-Camacho et al., 2013). Briefly, antigen retrieval was performed by boiling the slides at 120°C for 25 min in 10 mM Sodium Citrate buffer pH 6.0 (Sigma). After washing with Tris-buffered saline (TBS) buffer containing 0.1% (v/v) Tween-20 (TBST), permeabilization and blocking were performed by incubating the sections at 4°C for 12 hr with a blocking solution containing 10% normal horse serum, 1% BSA, 0.1% gelatin and 0.3 M glycine in TBST. Endogenous peroxidase activity was blocked by incubation with 0.3% hydrogen peroxide (Sigma) in TBS 30 min at RT. Then, the slides were washed and incubated with blocking solution containing 1% normal horse serum, 1% BSA, 0.1% gelatin and 0.3M glycine in TBST. After incubating with the primary antibody for 24 hr at 4°C, slides were washed and incubated with the biotinylated secondary antibodies 1 hr at RT. Primary and secondary antibodies used for IHC are described in the Key Resources Table. The slides were washed and incubated for 1 hr in the ABC solution (Vectastain Elite ABC kit, Vector Laboratories), and developed by using the ImmPACT™ DAB Peroxidase Substrate Kit (Vector Laboratories). Optionally the slides were stained with hematoxylin and Congo Red (see protocol below), dehydrated and mounted with DPX mounting medium (Sigma). Representative images were obtained using the Leica DM 2500M light microscope.

AT8 and MC1 IHC were performed in serial sections with STEM121 IHC intended to determine the area of the human graft. AT8 and $MC1^+$ signals were analyzed as mouse host tissue or human grafted cells depending on the location of $STEM121^+$ signals.

Electron Microscopy and Immunogold

The mice intended for EM analysis were perfused with 0.1 M phosphate buffer (PB) followed by fixative solution (2% paraformaldehyde, 2.5% glutaraldehyde in 0.1 M PB pH 7.4). Brains were removed, stored in the same fixative solution 3-4 days at 4°C and then cut into 60 μm slices on a Leica VT1000S vibratome. Areas comprising either the xenografts or the host tissue were dissected and further processed for EM as described previously (Arranz et al., 2015). Briefly, tissue was washed overnight in PBS and post-fixed for 2 hr at RT with 1% OsO_4, 1.5% $K_4Fe(CN)_6$ in 0.1 M PB. Sections were then rinsed and stained with 3% uranyl acetate for 1 hr at 4°C. Dehydration was performed on ice by transferring the sections to 35%, 50%, 70%, 90% and 2 steps of 100% ethanol, followed by 2 steps of propylene oxide. The sections were embedded in EMbed812. Resin blocks comprising the xenografts or the host tissue were sectioned on an ultramicrotome (Leica Ultracut UCT, Leica Microsystems). Semithin sections (1 μm) were collected on slides and stained with 1% Toluidine blue solution (Sigma-Aldrich) and mounted in VectaMount mounting medium (Vector). Representative areas were imaged under a light microscope (Leica DM 2500M). Ultrathin sections (70 nm) were mounted on copper grids and imaged using a JEM-1400 transmission electron microscope (JEOL), equipped with an 11Mpixel Olympus SIS Quemesa camera or with a Zeiss EM 809 transmission electron microscope.

When immunogold detection was needed, the mice were perfused with a different fixative (2% paraformaldehyde and 0.2% glutaraldehyde in 0.1 M PB pH 7.4). For immunolabelling, 60 μm brain sections were first treated with 0.1% sodium borohydride for 30 min, washed and incubated in blocking solution (4% goat serum in PBS) for 1 hr. After incubating with the primary antibodies (rabbit GFP or mouse STEM121), sections were washed in 0.1% fish gel, 0.2% BSAc in PBS 2 times for 10 min. Sections were incubated with the corresponding secondary antibodies (goat anti-mouse or goat anti-rabbit IgG conjugated to ultra-small gold particles of 0.8 nm) diluted in 0.1% fish gel, 0.2% BSAc in PBS for 4 hr at RT. After post-fixation in 1% glutaraldehyde for 10 min, the immunogold signal was intensified using a silver enhancement kit (HQ silver; Nanoprobes). Further processing of the tissue for EM was performed as explained above.

Aβ plaque Stainings

Aβ plaques were detected either by immunostaining using 6E10 (Key Resources Table), or by staining with Thioflavin (SIGMA) or Congo Red (SIGMA) to detect β sheet (aggregated state) conformations, as described previously (Radde et al., 2006). Briefly, for Thioflavin staining brain sections were incubated with a filtered 0.05% aqueous Thioflavin-S (SIGMA) solution in 50% ethanol for 5 min at RT. After rinsing gradually with 70%, 95% ethanol and water, the sections were mounted with Glycergel (DAKO). When Congo Red (SIGMA) was used to detect Aβ plaques, paraffin slides were dipped with 1% Sodium Chloride Solution for 20 min at RT followed by incubation in 1% Congo Red solution for 20 min. The slides were then dehydrated followed by xylene treatment and covered with DPX mounting medium (Sigma-Aldrich).

TUNEL Apoptosis Assay

We used the Apop Tag Plus In situ apoptosis Fluorescein Detection Kit (Chemicon/Millipore) to detect apoptotic cell death. Vibratome sections were first treated for antigen retrieval and immunostaining was performed as described above. Sections were then immersed in 0.9% NaCl, washed and fixed in 4% paraformaldehyde. Sections were treated with proteinase K, washed, and post-fixed in a mix of ethanol: acetic acid (2:1) at -20°C. Sections were incubated with the Working Strength TdT enzyme for 1 hr at 37°C. Next, sections were incubated with the Working Strength Stop/Wash Buffer at RT. Last, the Anti-Digoxigenin conjugate was applied to the samples at RT. Sections were stained with DAPI and mounted on slides with Glycergel (DAKO).

Graft Dissection and RNA Extraction

Mice were sacrificed and quickly decapitated. The brain was dissected around the midbrain and the rostral part containing the cortex was fixed to a platform for vibratome slicing into 300 μm brain sections at low speed 1, frequency 7-8. The buffer used was ice-cold artificial CSF (Sucrose 212.5 mM; KCl 3.5mM; NaHCO3 16mM; KH_2PO_4 1.2mM; Glucose 10mM; $CaCL_2$ 1mM; $MgCl_2$ 3mM) (SIGMA), after CO_2 equilibration. Slices were kept in artificial CSF/CO_2 and further processed under a binocular fluorescence microscope to dissect the GFP^+ human graft tissue. Tissue pieces containing the human graft were collected into RNase free tubes and were snap frozen in liquid nitrogen. Total RNA material was extracted using the QIAGEN Kit RNA easy, and eluted in RNase free water. RNA concentration (ng/μl) and purity/quality (ratios 260/280 and 260/230) were quantified using Nanodrop spectrophotometer technology.

RNA-seq Data Discrimination of Human Sequences in the Mixed Human + Mouse Sample

To ensure that we can reliably do RNA-seq on a sample containing both mouse and human RNA we mapped three datasets to mouse, human and a mouse + human database. The three RNA-seq datasets we used were derived from:

1. Human brain samples, 50bp read length, single end (own data, not published).
2. Mouse hippocampus, 76bp read length, single end (own data, not published).
3. Simulated human data 100bp read length, single end (based on the human hg19 genome).
4. Simulated mouse data 100bp read length, single end (based on the mouse mm10 genome).

Each dataset is mapped to the mixed database and depending on the origin, the corresponding human or mouse only database, using STAR RNA-seq aligner (Dobin et al., 2013) (same version, same parameters as used in this paper). For each mapping the number of reads mapping with a quality score > 10 to each database genome was determined. This yielded the following data:

Sample	Raw Reads	Mapped to Database	Mapped to Organism		% Mapped	
			hg19	mm10	hg19	mm10
A	2,069,030,113	hg19	1,393,960,897	N/A	67.4%	N/A
A	2,069,030,113	hg19+mm10	1,347,734,447	10,196,128	65.1%	0.5%*1
B	210,668,268	mm10	N/A	188,764,921	N/A	89.6%
B	210,668,268	hg19+mm10	141,165	162,975,781	0.1%*1	77.4%
C	193,082,054	hg19+mm10	188,047,214	2	97.4%	0.0%*2
D	16,237,465	hg19+mm10	14	15,618,208	0.0%*2	96.2%

Cross-Mapping

One major concern when mapping a mix of human + mouse RNA to a RNA-seq database containing both human and mouse is that reads might accidentally map to the wrong genome. These results show that the percentage of cross mapping reads is very low. The (non-simulated) human and mouse material show a cross-mapping ratio of 0.5% and 0.1% (*1). The simulated human and mouse material do not cross-map at all (*2). The difference between the simulated and non-simulated data can be explained by (a) the non-simulated data has shorter read lengths (also shorter than the 100bp used in the paper) and (b) the fact that real biological data will contain genomic differences to the reference genome, adding to the potential to cross-map. It is therefore logical to assume that the cross-map percentage for the experiment in this paper will be better than the biological samples (A+B, due to the longer read length), but not as good as the artificial samples (C+D, due to the genomic variation).

Fraction of Reads Mapping

By selecting only reads that map with a quality score of 10 or better, we strongly select against reads which cannot be mapped to a unique location in the genome (using either the organism specific database or the mixed database) preventing cross-mapping. It is however possible that this drastically reduces the number of reads able to map, and hence reduces sensitivity of measuring of expression. We can assess this by checking how many reads map (of sample A+B) when mapped to the corresponding genome, and compare these numbers to the number of reads mapping to the mixed database. For sample A (human) we lose 2.3% of all reads (67.4%–65.1%). In the mouse sample we lose 12.2% (89.6%–77.4%). However, in both cases a very respectable amount of reads is still able to map uniquely to the genome. This data shows that it is possible to reliably map an RNA-seq dataset derived from mixed human and mouse sample.

QUANTIFICATION AND STATISTICAL ANALYSIS

Morphological Analysis for Quantification

Morphometry and measurements were performed with Fiji/ImageJ software. For quantifications, at least 4-5 different brain sections comprising the human xenografts and the adjacent mouse host tissue were included per animal.

Immunofluorescence (IF) sections were imaged by confocal microscopy (Nikon Ti-E inverted microscope) with a 20x (0.75 NA) objective to image Z series stacks of areas inside human xenografts or mouse host tissue (8-10 optical sections 1 μm apart for each image). All images were acquired using identical acquisition parameters as 16-bit, 1024x1024 arrays. Z series stacks were then converted in Fiji/ImageJ to maximum intensity projections and threshold adjusted to isolate specific fluorescence.

Immunohistochemistry (IHC) sections were imaged using a Leica DM 2500M light microscope with a 63x objective. All images were acquired using identical acquisition parameters as 16-bit, 1024x1024 arrays.

Ultrathin EM sections comprising either the human xenografts or the adjacent mouse host tissue were imaged using a JEM-1400 transmission electron microscope (JEOL) equipped with a 11M-pixel Olympus SIS Quemesa camera. Images were taken in randomly selected areas at a 600x magnification.

Quantification of Aβ Plaque Burden

The mean area of Aβ plaques and the number of Aβ plaques per area was manually determined on IF images using Fiji/ImageJ. Results are shown for mouse host (n = 5) and human grafts (n = 5) in AD mice 4MPT. Data are represented as mean ± SEM. Statistical analysis were done with Student's t test.

Statistical details of experiments can be found in Figure 1 and related figure legend.

Quantification of Neuroinflammation

The number of Iba1$^+$ and GFAP$^+$ cells per area was quantified manually on IF images in 4 different blindly set areas. Results are shown for mouse host from WT mice (n = 3 animals 4MPT; n = 4 6MPT); mouse host from AD mice (n = 3 animals 4MPT; n = 4 6MPT); human grafts from WT mice (n = 3 animals 4MPT; n = 4 6MPT); human grafts from AD mice (n = 3 animals 4MPT; n = 4 6MPT). Data are represented as mean ± SEM. Statistical analysis was done with two way-ANOVA with Bonferroni posttests.

The percentage of hypertrophic and/or phagocytic astrocytes and microglia cells was calculated on EM images manually with Fiji/ImageJ. Results are shown for human grafts in WT mice (n = 3) and human grafts in AD mice (n = 3) 6MPT. Data are represented as mean ± SEM. Statistical analysis were done with Student's t test.

Statistical details of experiments can be found in Figure 2 and related figure legend.

Quantifications of Ubiquitin+, SYP+, and VGlut1+ DNs

The percentage of Aβ plaques surrounded by Ubiquitin$^+$, SYP$^+$ and VGlut1$^+$ DNs was manually determined on IF images using Fiji/ImageJ. Ubiquitin results are shown for mouse host from AD mice (n = 5) and human grafts from AD mice (n = 5). SYP and VGlut results are shown for mouse host from AD mice (n = 5) and human grafts from AD mice (n = 5 and n = 4, respectively). Data are represented as mean ± SEM. Statistical analysis were done with Student's t test.

Statistical details of experiments can be found in Figure 3 (for Ubiquitin), Figure 4 (for SYP and VGlut) and related figure legends.

Quantification of Cell Density

Aβ plaques on IF images were visualized as masks (examples of Aβ masks used for Figures 5E and 5K shown in Figures S4G and S4H) and consequently a total area from the center of the plaque was drawn, akin to a Scholl analysis but with variable borders. The area was increased from the original detected mask of the plaques by a factor 50. Touching areas were fused and areas were calculated at each step. Nuclei were counted manually inside the areas and cell density was expressed as the number of nuclei per area. Data is represented as the % of relative cell density of AD versus WT mice. Quantification was performed at 2MPT or 6MPT: human grafts/AD mice (n = 4 mice 2MPT; n = 4 6MPT); human grafts/WT mice (n = 3 mice 2MPT; n = 4 6MPT); mouse host/AD mice (n = 4); mouse host/WT mice (n = 4); human Tau* grafts/AD mice (n = 3 mice 6MPT); human Tau* grafts/WT mice (n = 3 mice 6MPT). Data are represented as mean ± SEM. Statistical analysis was done following one way-ANOVA with Bonferroni posttests.

In addition, the neuronal density and the percentage of degenerating necrotic neurons were calculated manually on EM images using Fiji/ImageJ. Results are shown for mouse host in WT mice (n = 3), mouse host in AD mice (n = 3), human grafts in WT mice (n = 3) and human grafts in AD mice (n = 3). Data are expressed as mean ± SEM. Statistics were performed by two way-ANOVA with Bonferroni posttests.

Statistical details of experiments can be found in Figure 5 and related figure legend.

Quantification of the Percentage of 4R Tau+ Cells

The percentage of 4R Tau$^+$/GFP$^+$ cells (in human grafts) or 4R Tau$^+$/HuNCAM$^+$ cells (in human Tau* grafts) was manually determined on IF images using Fiji/ImageJ. Results are shown for human grafts 4MPT (n = 3) and 6MPT (n = 6 mice); human Tau* grafts 4MPT (n = 4) and 6MPT (n = 2 mice). Data are expressed as mean ± SEM. Statistical analysis was done following two way-ANOVA with Bonferroni posttests.

Statistical details of experiments can be found in Figure 6 and related figure legend.

Quantification of the Percentage of Aβ Plaques Surrounded by AT8 or MC1$^+$ DNs

The proportion of Aβ plaques surrounded by AT8$^+$ or MC1$^+$ DNs was determined manually on IHC images with Fiji/ImageJ. Results are shown for human grafts (n = 4 mice), human Tau* grafts (n = 3) and mouse host tissue (n = 3) in AD mice. Data are represented as mean ± SEM. Statistical analysis was done following one-way ANOVA with Kruskal-Wallis test.

Statistical details of experiments can be found in Figure 7 and related figure legend.

RNA-Seq Data Analysis

RNA samples of high quality and high RIN values (8-10) (RNA stability) were used for this study. 7 samples containing human grafted cells transplanted into AD animals and 7 samples of human grafted cells transplanted into WT animals were analyzed 4-5MPT. 5 samples containing human grafted cells transplanted into AD animals and 2 samples of human grafted cells transplanted into WT animals were analyzed 8MPT. The extracted RNA was analyzed by the VIB nucleomics core (http://www.nucleomics.be/) which generated polyA RNA-seq libraries using the Illumina Truseq stranded mRNA library prep protocol (Protocol 15031047 Rev E_October 2013). The libraries were sequenced on an Illumina Nextseq 500 sequencer, generating 100bp single-end reads. Raw reads were mapped to a combined database of the mouse (GRCm38/mm10) and human genome (hg19, gencode19) using the STAR RNA-seq aligner (version 2.4.2a) (Dobin et al., 2013). Raw read counts were determined using the FeatureCounts software (Liao et al., 2014) with a GTF file combining the human and mouse annotation with an alignment quality cutoff of 10.

Differential Expression Analysis

Prior to differential expression analysis we performed a PCA analysis on the normalized counts and manually removed obvious outliers (leaving a total of 7 AD samples, 5 WT samples at 4-5MPT and 5 AD samples, 2 WT samples at 8MPT). Sequenced RNA from the combined mouse & human material was mapped back to a joint database of the human and mouse genome. The genomic differences between mouse and human allowed us to reliably separate human from mouse reads (explained above) and perform an independent differential expression analysis of the human and mouse expression data in both the young and old mice. Differential expression analysis was performed for the early and late stage samples using edgeR (Robinson et al., 2010) comparing samples from APP/PS1 mice to WT mice.

Enrichment Analysis

A set of GO categories related to AD was collected based on the GO ontology (2016-02-10) and human gene annotations (2016-02-16). GO categories related to AD were manually selected excluding overlapping, as well as small and large sets. Co-expression gene sets as defined by (Zhang et al., 2013) were extracted from their supplemental data. To assess to what extent the expression patterns from our human neurons are comparable to the networks identified by Zhang et al., we performed a co-expression clustering analysis using WCGNA (Langfelder and Horvath, 2008) on our data. This approach yield modules of genes showing a similar expression pattern across samples, comparable to the modules identified by Zhang et al. To perform the WCGNA analysis we used the normalized counts from the differential expression analysis as input and filtered out the lowest expressing genes, leaving 14632 genes. We then run WCGA with the power parameter set to 5. This yields 33 gene modules. To more directly compare the differential expression results, we add 4 gene sets containing the 1000 most up and downregulated genes from the young and old mice. The overlap of genes of these 37 modules with all modules identified by Zhang et al. is determined by a fisher exact test, with as background all genes which are a part of both our modules as well as the Zhang modules. The p values of the 2442 comparisons are corrected for Multiple testing using the Benjamini Hochberg (Benjamini and Hochberg, 1995) approach.

Determination of Tau Splice Form Usage

Raw junction counts as generated by the STAR aligner (Dobin et al., 2013) were collected. The raw junction counts were normalized for library size using Limma Voom (Ritchie et al., 2015). From the complete table of splice forms the normalized junction counts of MAPT exon 9-10 ($X_{9,10}$, hg19, chr17, position 44074031 to 44087675), 9-11 ($X_{9,11}$, chr17, position 44074031 to 44091608) and 10-11 ($X_{10,11}$, chr17, position 44087769 to 44091608) were extracted. The 3R splice form is represented by the junction 9-11 and 4R by both 9-10 and 10-11. The percentage of MAPT 4R usage was subsequently calculated by: $100 * (X_{9,11}) / (0.5 * (X_{9,10} + X_{10,11}))$ and visualized in a boxplot. A total of 7 AD samples and 5 WT samples at 4-5MPT; and 5 AD samples, and 2 WT samples at 8MPT were used for the analysis.

DATA AND SOFTWARE AVAILABILITY

RNA-seq raw read counts determined by Featurecount software of human PSC-derived neurons grafted into the cortex of AD and WT mice are available in Table S6. RNA-seq raw read counts determined by Featurecount software of murine AD and WT cortex are available in Table S7. The Software tools used for the RNA-seq analysis in this study are the following: STAR RNA-seq aligner (Dobin et al., 2013), available in https://github.com/alexdobin/STAR; Subread/Featurecounts (Liao et al., 2014), available in http://subread.sourceforge.net/; Pandas Python Data Analysis Library, available in http://pandas.pydata.org/; Limma / Linear Models for Microarray Data, (Ritchie et al., 2015), available in https://bioconductor.org/packages/release/bioc/html/limma.html; and Benjamini-Hochberg algorithm (Benjamini and Hochberg, 1995).